Pattern dynamics of parametrically excited spin waves near the instability threshold

Franz-Josef Elmer
Institut für Physik, Universität Basel, CH-4056 Basel, Switzerland
(Received 14 December 1995)

The dynamics of dissipative patterns built up by parametrically excited spin waves in an insulating ferromagnetic film driven by out-of-plane parallel pumping is studied theoretically. Crystal-field anisotropies and surface pinning of spins are neglected whereas the dipolar field is fully included. Near the instability threshold the dynamics are governed by amplitude equations for the slowly time-varying amplitudes of pairs of unstable spin waves. Because of rotational symmetry an infinite number of spin waves having the same wavelength but propagating in different directions become unstable simultaneously. The dynamics of the amplitude equations is mainly determined by a nonlinear coupling coefficient which is not an even function of the difference between the angles of propagation. A detailed description of the numerical method of the calculation of the coefficients of the amplitude equations is given. From the amplitude equations stationary solutions and their stability are calculated. The only stable patterns are squares and three-wave patterns; hexagons are unstable. For frequencies of the pump field above some threshold all stationary patterns are unstable. In this regime the dynamical behavior is dominated by switching between squares and/or three-wave patterns. The pattern switching is extremely sensitive to noise which leads to a weak noise-induced turbulence. [S0163-1829(96)05122-3]

I. INTRODUCTION

Pattern formation in systems driven far from thermal equilibrium has universal features which can be found in many different physical, chemical, and even biological system (for a review see Ref. 1). Most of the physical systems which have been studied experimentally as well as theoretically are fluids driven in various ways. The reason for that is twofold. First, the basic macroscopic equation of motion of a simple fluid, the Navier-Stokes equation, have been well known for more than 150 years. This equation is well established and its limits are very well known. It is the foundation on which all theoretical studies rely. But the main reason for the popularity of fluids is that it is easy to *visualize* the patterns and their formation.

This visualization gives important information about the state of the system which fruitfully stimulates theoretical approaches. The theories lead to predictions which can often be tested in relatively cheap experiments. Thus the visualization of the pattern formation in fluids leads to a strong interaction between theory and experiment which is an important factor for a successful understanding of pattern formation.

But how typical is pattern formation in fluids for nonequilibrium pattern formation in general? Which behaviors are universal? In order to answer these questions, totally different systems were studied and still have to be studied. In this paper I investigate insulating solid-state ferromagnets well below the Curie temperature. There are well-known systems for nonlinear pattern formation in thermal equilibrium.[2] Ferromagnets can be driven away from thermal equilibrium by fast oscillating electromagnetic fields.

In 1952 a nonequilibrium effect in ferromagnets driven in this way was found by Bloembergen and Damon.[3] They observed an anomalous behavior in the ferromagnetic resonance if the strength of the driving microwave (pump field) exceeds some threshold. In 1957 Suhl was able to explain successfully this typical nonequilibrium effect by *parametric resonance* of spin waves.[4] In the last ten years high-power ferromagnetic resonance has become a well-known example for deterministic chaos in a solid-state system.[5]

The nonlinear dynamics of parametrically excited spin waves is mostly investigated by means of traditional ferromagnetic resonance techniques. These methods are unable to visualize the patterns which emerge above the threshold; they provide only *spatially averaged* information about them. There are a few experiments reported in the literature where inelastic Brillouin scattering was used to investigate these patterns.[6,7] But this method is also unable to visualize patterns in real space because of the inelastic character of the scattering. The lack of visualizations of pattern formation in high-power ferromagnetic resonance is a major disadvantage compared to fluid systems.

What is an appropriate method of visualization of parametrically excited spin waves? Equilibrium patterns in micromagnetism can be visualized very well with *Faraday rotation* because the rotation of the polarization of a light beam penetrating a sample depends on the component of the magnetization parallel to the beam. This method has also been successfully applied in the measurement of precession cones in ferromagnetic resonance.[8]

In order to have optimal experimental conditions of visualization, a *film* with the static field perpendicular to the film plane would be ideal. The reasons for that are twofold. First, in a film the pattern is quasi-two-dimensional. Second, the static field should be parallel to the light beam in order to measure the precession cone as optimally as possible. From the experimental point of view either parallel or transverse pumping is appropriate. In this paper only parallel pumping is investigated because of simplicity.

The aim of this paper is to investigate and to predict spin-wave patterns and their dynamics in a system which is optimized as above in order to get good chances for successful

pattern visualization. Because of simplicity a very ideal film is studied. It is a uniform one without inhomogeneities and impurities. In the (x,y) plane it extends to infinity with an overall constant thickness. The only intrinsic fields are an isotropic exchange field and the dipolar field. Furthermore, the surface spins are assumed to be free. Crystal-field anisotropies and surface pinning of the spins are neglected. This is not a matter of principle. The restriction is introduced only for simplicity; the theory presented below can be easily extended in this direction.

It is very helpful especially for the discussion of universal aspects of pattern formation to compare out-of-plane parallel pumping with two pattern-forming systems from fluid dynamics. The first system is the *Faraday instability* observed in 1831 by Faraday.[9] It is a parametric resonance instability of surface waves on a fluid which is driven by a vertical oscillation of the fluid container. Squares, stripes, hexagons, and spatially quasiperiodic patterns, as well as defects in these patterns have been observed.[1] The similarity to the out-of-plane parallel pumping of a ferromagnetic film is evident because of parametric resonance. Furthermore both systems are in the ideal case translationally and rotationally symmetric. The latter symmetry has the consequence that at the instability threshold a continuous set of waves with the same wavelength but propagating in different directions become unstable at once. Nonlinear interaction between these waves is responsible for the kind of patterns the system will select. In the case of the Faraday instability this leads mainly to squares.[10] In the case of out-of-plane parallel pumping I have predicted squares and three-wave patterns.[11]

The general behavior of a pattern forming system is strongly influenced by symmetries. They are important sources of universalities. From this point of view one recognizes an essential difference between Faraday instability and spin-wave instability. The fluid system has an additional symmetry which is strongly broken in the magnetic system: the reflection symmetry at an arbitrary plane perpendicular to the surface. The reason for the symmetry breaking is the magnetic field, more precisely, the dipolar field which is also responsible for the parallel pumping instability.

For that reason I compare pattern formation in out-of-plane parallel pumping also with another well-studied fluid system where the reflection symmetry is also broken but which is still translationally and rotationally symmetric. It is the *rotated* Rayleigh-Bénard system. The rotation breaks the reflection symmetry. When the angular velocity is below a threshold, the system behaves like a nonrotated Rayleigh-Bénard convection where convection rolls appear for Rayleigh numbers (i.e., for temperature differences) which are larger than a critical value. But above the threshold these roll patterns are unstable even at the onset of convection. This is the Küppers-Lortz instability.[12] In 1980 Busse and Heikes analyzed the consequence of this instability based on the investigation of a system of three coupled amplitude equations.[13] They found that when a new convection roll grows due to the Küppers-Lortz instability the old roll disappears simultaneously. Thus one roll pattern is switched off and at the same time a new roll pattern, rotated by a finite angle (roughly 60°), is switched on. They also did experiments which seemed to confirm this analysis. I have shown that this *pattern switching* should also occur in out-of-plane parallel pumping.[14] From the general point of view the reason for pattern switching in both systems is the lack of reflection symmetry.

The starting point of the present theoretical investigation is the basic equation of motion of micromagnetism, i.e., the Landau-Lifshitz equation. In a first step the stability of the ground state is calculated. At the instability threshold of parametric resonance nontrivial solutions bifurcate. In leading order these solutions are linear superpositions of the destabilizing spin waves. In a second step a system of *amplitude equations* for the amplitudes of the standing spin waves is derived in the framework of multiple-scale perturbation theory where the smallness parameter is the distance from the threshold.

It is very common to investigate pattern formation in terms of amplitude equations.[1,15] The advantage is twofold. First, from the point of view of bifurcation theory they are normal forms and can therefore be rigorously derived. For that reason they are universal which means that their form is determined completely by symmetry and the kind of symmetry breaking caused by the instability. All other properties of the system are condensed into a few coefficients. The second advantage is that pattern formation can be investigated even though the coefficients of the amplitude equations are not known explicitly either because the basic equation is not known or because it is to difficult to derive the coefficients.

The approach presented in this paper is different from approaches found in the literature of spin-wave instabilities.[5] The most systematic one is the S theory.[16,17] In the language of pattern formation the S theory is a multiple-scale perturbation theory. It starts from the *undamped* system. The smallness parameter is the strength of the parametric driving. The resulting equation of motion describes the dynamics of the amplitudes of all spin waves (i.e., solutions of the linearized, undamped, undriven system) fulfilling the parametric resonance condition (i.e., frequency of spin waves equals half the driving frequency). Damping is introduced phenomenologically into the equations of motion. It is not related to the Landau-Lifshitz damping. Amplitude equations can also be derived from the equations of motion of the S theory. Milner has successfully applied this two-step approach (i.e., basic equation of motions $\rightarrow$ S theory $\rightarrow$ amplitude equations) for the Faraday instability.[10]

The main reason for starting directly from the Landau-Lifshitz equation is that the S theory is applicable only for small damping constants, because the threshold for parametric resonance scales linearly with the damping constant. Another disadvantage is that the S theory does not include the damping in a systematic way. But linear and nonlinear damping terms have strong influences on pattern formation.[10]

An attempt to study pattern formation in high-power ferromagnetic resonance in terms of amplitude equations was done by the author several years ago.[18,19] A general discussion of the possible forms of amplitude equations in terms of symmetry was given by the author in Ref. 20. Very recently Matthäus and Sauermann derived amplitude equations for a ferromagnet with an uniaxial internal anisotropy field but with dipolar field neglected.[21] In the present work the dipolar field is fully included. The amplitude equations are derived, their coefficients are calculated, and their solutions are discussed. The main results have been previously published in

two short communications.[11,14]

The paper is organized in the following manner. The basic equations of motions are presented in Sec. II. In Sec. III the stability of the ground state is calculated numerically as well as in an analytical approximation. In Sec. IV the amplitude equations are derived. The stationary solutions of the amplitude equations as well as their stability are investigated in Sec. V. The dynamical behavior of the amplitude equations are discussed in Sec. VI. In the last section (Sec. VII) the results are summarized and their relevance for experiments are discussed. Also concluding remarks concerning extensions of the theory in various directions are given.

II. THE BASIC EQUATIONS OF MOTION

Static magnetization patterns are very well described by the theory of micromagnetism.[2] They are local minima of the free energy W. Micromagnetism assumes that the temperature is much below the Curie temperature and that typical length scales of the patterns (e.g., the width of a domain wall) are much larger than the atomic scale (e.g., the diameter of the crystallographic unit cell). The state of a ferromagnet is therefore determined by the magnetization field $\mathbf{M}(\mathbf{r})$. Its dynamics is governed by the Landau-Lifshitz (LL) equation,

$$\frac{1}{\gamma}\partial_t \mathbf{M} = -\mathbf{M}\times\mathbf{H}^{\mathrm{eff}} - \frac{g}{M_0}\mathbf{M}\times(\mathbf{M}\times\mathbf{H}^{\mathrm{eff}}), \tag{1}$$

where γ is the gyromagnetic ratio, M_0 is the value of the magnetization in thermal equilibrium, $\mathbf{H}^{\mathrm{eff}}(\mathbf{r},t) = -\delta W/\delta \mathbf{M}$ is the effective magnetic field at site $\mathbf{r}$, and g is the relative line width of the resonance line. The LL equation will be our basic equation of motion like the Navier-Stokes equation for fluid dynamics.

The damping term of the LL equation (i.e., the second term on the right-hand side) is a phenomenological one. In the literature other damping terms are also used. The most common ones are (i) the Gilbert damping $(g/\gamma M_0)\mathbf{M}\times\partial_t\mathbf{M}$, which is mathematically equivalent to the Landau-Lifshitz damping and (ii) the Bloch-Bloembergen damping $\Gamma_\perp M_x \mathbf{e}_x + \Gamma_\perp M_y \mathbf{e}_y + \Gamma_\parallel (M_z - M_0)\mathbf{e}_z$, which is mainly used in connection with ferromagnetic resonance. Only the Landau-Lifshitz and Gilbert damping leave the length of magnetization vector unchanged (i.e., $|\mathbf{M}| = M_0 = \mathrm{const}$).

In theories of parametrically excited spin waves, damping is usually introduced in another phenomenological way.[5,16,22] The magnetization is described by a superposition of spin waves. The dynamics is governed by a equations of motion for the amplitudes of the spin waves. They are derived from the *undamped* LL equation. Damping is introduced by adding phenomenological damping terms. Their coefficients are assumed to depend on the wave number. The coefficient of the linear term can be obtained from measurements of the threshold of parallel pumping.[22] These measurements are not consistent with the coefficient one would get from the LL equation. From this point of view the damping term in the LL equation should be replaced by a spatial convolution term. But $\mathbf{M} = \mathrm{const}$ and the correct wave-number dependence of the linear damping term do not determine it uniquely. Such a generalized damping term can be derived only from a microscopic theory.[23,24] Nevertheless we use in this paper the LL equation (1) because we want to demonstrate our method for a simple case. A second reason is that the state of the art in visualization of a parametrically excited spin-wave pattern is far from the point where an accurate quantitative comparison between theory and experiment is possible.

The LL equation has to be completed by the specification of $\mathbf{H}^{\mathrm{eff}}$,

$$\mathbf{H}^{\mathrm{eff}} = (H + h\cos\tilde{\omega}t)\mathbf{e}_z + D\nabla^2\mathbf{M} - \nabla\Phi_M . \tag{2}$$

The first term is the external field; the second term comes from the exchange interaction; the third term is the dipolar field where electromagnetic wave propagation has been neglected. The dipolar field is the gradient of the magnetostatic potential Φ_M which obeys Poisson's equation,

$$\Delta\Phi_M = \begin{cases} 4\pi\nabla\mathbf{M}, & \text{inside the sample,} \\ 0, & \text{outside the sample.} \end{cases} \tag{3}$$

We assume a film of thickness d infinitely extended in the (x,y) plane. The boundary conditions are

$$|\nabla\Phi_M|(|z|\to\infty) = \partial_z\mathbf{M}|_{z=0} = \partial_z\mathbf{M}|_{z=d} = 0. \tag{4}$$

This Neumann-like boundary conditions for the magnetization are caused by the fact that we assume free surface spins. In the case of strong surface pinning the boundary conditions would be Dirichlet-like.

Since the length of the magnetization vector is invariant under the dynamics, the number of independent components of $\mathbf{M}$ is two rather than three. The magnetization is defined by a point on the sphere with radius M_0. It is convenient to project this sphere stereographically onto the (x,y) plane. Interpreting each point in this plane as a complex number, the magnetization reduces to a complex field $m(\mathbf{r},t)$ which is defined by

$$m = \frac{M_x + iM_y}{M_0 + M_z}. \tag{5}$$

The transformation back to $\mathbf{M}$ reads

$$\mathbf{M} = \frac{M_0}{1+|m|^2}\begin{pmatrix} m+m^* \\ im^* - im \\ 1-|m|^2 \end{pmatrix}. \tag{6}$$

The LL equation in terms of m reads[25]

$$\partial_t m = (i-g)\left[-l^2\Delta m + 2l^2\frac{m^*(\nabla m)^2}{1+|m|^2} + \frac{1}{2}(\partial_x + i\partial_y)\phi_M - \frac{m^2}{2}(\partial_x - i\partial_y)\phi_M + m(\omega_H + \omega_h\cos\omega t - \partial_z\phi_M)\right]. \tag{7}$$

We have introduced the following dimensionless time and space units:

$$t \to \frac{t}{4\pi\gamma M_0}, \quad \mathbf{r}\to\mathbf{r}d \tag{8}$$

and parameters

$$l=\frac{1}{d}\sqrt{\frac{D}{4\pi}},\quad \phi_M=\frac{\Phi_M}{4\pi M_0 d},$$

$$\omega_H=\frac{H}{4\pi M_0},\quad \omega_h=\frac{h}{4\pi M_0},\quad \omega=\frac{\tilde{\omega}}{4\pi\gamma M_0}. \tag{9}$$

The Poisson equation (3) becomes

$$\Delta\phi_M=(\partial_x+i\partial_y)\left(\frac{m^*B(z)}{1+|m|^2}\right)+(\partial_x-i\partial_y)\left(\frac{mB(z)}{1+|m|^2}\right)$$
$$+\partial_z\left[\left(\frac{1-|m|^2}{1+|m|^2}\right)B(z)\right], \tag{10}$$

where $B(z)$ is the box function

$$B(z)=\begin{cases}0, & \text{for } z<0,\\ 1, & \text{for } 0\leqslant z\leqslant 1,\\ 0, & \text{for } z>1.\end{cases} \tag{11}$$

The advantage of writing the Poisson equation with the box function is that we do not need to distinguish between inside and outside of the sample. Furthermore the correct boundary condition for the dipolar field at the surface is automatically fulfilled. The boundary conditions (4) turn into

$$|\nabla\phi_M|(|z|\to\infty)=\partial_z m|_{z=0}=\partial_z m|_{z=1}=0. \tag{12}$$

Note that the boundary condition for m would be nonlinear in the case of surface pinning of the spins.

Equations (7) and (10) together with the boundary condition (12) represent the basic equations of motion from which we will start our investigation. There are five independent parameters: The exchange length l measured in units of the film thickness, the damping constant g, the static field ω_H and the pump field ω_h measured in units of the demagnetization field (i.e., $4\pi M_0$), and the frequency of the driving field measured in units of $1/(4\pi\gamma M_0)$.

III. THE INSTABILITY OF THE GROUND STATE

The trivial stationary state of (7,10,12) is

$$m^T=0,\quad \phi_M^T=\frac{|z|-|z-1|}{2}, \tag{13}$$

where the magnetization **M** is parallel to the external field. The magnetostatic potential ϕ_M^T causes the dipolar field $-\nabla\phi_M^T=-\mathbf{e}_z$ which reduces the external static field ω_H. This demagnetization leads to the well-known instability of a uniformally magnetized sample against domain formations for $\omega_H<1$. In that case the trivial state (13) is not the ground state. We are not further dealing with this case. Therefore we assume that always $\omega_H>1$ holds. The trivial state (13) is then the ground state of the undriven system.

It is well known that in the bulk the ground state becomes unstable if the pump field exceeds some threshold. The destabilizing modes are spin waves which fulfill the parametric resonance condition (i.e., $\omega_k=\omega/2$) and propagate perpendicular to the external field.[22] But the boundaries make the subject more complicated. First they discretize roughly speaking the z component of the wave number. But, as we will see below, the bulk analysis is still correct in so far as the waves which are roughly uniform in z direction cause the instability. The only exception is related to the second effect of the boundaries, namely the *hybridization* (i.e., the avoiding of crossings of different branches) of waves with different z components in the wave number. Near a hybridization region the threshold of each wave will be increased which may allow another wave to become the most unstable one.

In order to study the stability of the ground state (13) we have to calculate whether an infinitesimally small deviation increases in time or dies out. Therefore the linearized equations of motion for the deviations m and $\phi=\phi_M-\phi_M^T$ has to be solved. They are

$$\partial_t m-(i-g)\Big[-l^2\Delta m+\frac{1}{2}(\partial_x+i\partial_y)\phi$$
$$+(\omega_H-1+\omega_h\cos\omega t)m\Big]=0 \tag{14a}$$

and

$$\Delta\phi-[(\partial_x+i\partial_y)m^*+\text{c.c.}]B(z)=0. \tag{14b}$$

The boundary conditions are still (12).

Equation (14a), its conjugated complex, and (14b) define a system of partial differential equations for m, m^*, and ϕ. This system is invariant under translation symmetry in the plane and rotation symmetry around the z axis. Since some coefficients are time periodic due to the driving field we make a Floquet ansatz:

$$\begin{pmatrix} m\\ m^*\\ \phi\end{pmatrix}(\mathbf{r},t)=\begin{pmatrix} e^{i\alpha}\mu(z,t)\\ e^{-i\alpha}\mu^*(z,t)\\ 2i\psi(z,t)/k\end{pmatrix}e^{i\mathbf{k}\mathbf{r}+\lambda t}, \tag{15}$$

where $\mathbf{k}=k_x\mathbf{e}_x+k_y\mathbf{e}_y$ is an arbitrary in-plane wave number with $k_x=k\cos\alpha$ and $k_y=k\sin\alpha$. The functions μ, μ^*, and ψ are solutions of

$$\partial_t\mu+\lambda\mu-(i-g)[-l^2\partial_z^2\mu+l^2k^2\mu$$
$$+(\omega_H-1+\omega_h\cos\omega t)\mu-\psi]=0, \tag{16a}$$

$$\partial_t\mu^*+\lambda\mu^*+(i+g)[-l^2\partial_z^2\mu^*+l^2k^2\mu^*$$
$$+(\omega_H-1+\omega_h\cos\omega t)\mu^*-\psi]=0, \tag{16b}$$

$$\partial_z^2\psi-k^2\psi-k^2(\mu+\mu^*)B(z)/2=0, \tag{16c}$$

with the boundary conditions

$$(\mu,\mu^*,\psi)(z,t+2\pi/\omega)=(\mu,\mu^*,\psi)(z,t),$$
$$\psi(|z|\to\infty)=0, \tag{17}$$
$$\partial_z\mu|_{z=0}=\partial_z\mu|_{z=1}=\partial_z\mu^*|_{z=0}=\partial_z\mu^*|_{z=1}=0.$$

It is often convenient to eliminate ψ by integrating (16c):

$$\psi(z,t)=-\frac{k}{4}\int_0^1 e^{-k|z-z'|}[\mu(z',t)+\mu^*(z',t)]dz'. \tag{18}$$

The imaginary part of λ is only determined up to integer multiples of ω, similar to the wave vector in the Bloch ansatz for the wave function of an electron in a crystal. We will restrict ourself to the first Brillouin zone $|\mathrm{Im}\lambda| \leqslant \omega/2$.

Equations (16) and (17) define an eigenvalue problem. The real part of the eigenvalues λ will tell us whether the ground state is stable or not. It is also important to know the unstable eigenfunctions, because in leading order the patterns emerging at the threshold are superpositions of these eigenfunctions. We call these eigenfunctions ''spin waves'' although they are strictly speaking not spin waves because they are the solution of the linearized but *driven* LL equation. For small values of g and ω_h the difference is not very large but important. It is therefore instructive to solve the eigenvalue problem for $g=\omega_h=0$.

A. Mode spectrum

We are looking for eigensolutions of the *undamped* (i.e., $g=0$) and *undriven* (i.e., $\omega_h=0$) eigenvalue problem (16) with boundary conditions (17). The eigenvalue λ is purely imaginary, i.e., $\lambda = i\omega_k$. Since the time-periodic term is absent, the eigenfunctions are constant in t. Appendix A shows the way to solve this eigenvalue problem exactly. But there remains a transcendental algebraic equation for ω_k which can be solved only numerically. Figure 1 shows the dispersion relation of several eigensolutions which are characterized by the number of nodes in z direction.

It is possible to get remarkably good results outside the hybridization area from an analytic approximation which works also very well for the stability thresholds. Furthermore a generalization of this approximation becomes the basis of the numerical treatment of the linear stability analysis and the calculation of the coefficients of the amplitude equations.

The approximation can be divided into three steps. First, we make the ansatz

$$(\mu,\mu^*)=(\mu_0,\mu_0^*)\cos(N\pi z), \tag{19}$$

where N is an integer denoting the number of *nodes* of the eigenfunction in z direction. This ansatz fulfills the boundary conditions (17). It also reflects the symmetry of the eigenvalue problem under reflection at the plane $z=1/2$. Second, we calculate ψ *exactly* by using (18). Note that ψ contains terms of the form $\exp(\pm kz)$ caused by the boundaries. In the third step we *project* ψ onto $\cos(N\pi z)$. That is, we multiply (18) with $\cos(N\pi z)$, integrate over z from zero to one, divide the result by $\int_0^1 \cos^2(N\pi z)dz$, and multiply the result again with $\cos(N\pi z)$. This leads to

$$\psi = -\beta_N(\mu_0+\mu_0^*)\cos(N\pi z) + \text{terms orthogonal to } \cos(N\pi z), \tag{20}$$

where

$$\beta_N=\frac{k}{1+\delta_{0N}}\int_0^1\int_z^1 e^{k(z-z')}\cos(N\pi z)\cos(N\pi z')dz'dz. \tag{21}$$

Here δ_{ij} is the Kronecker symbol. Calculating the integrals leads to

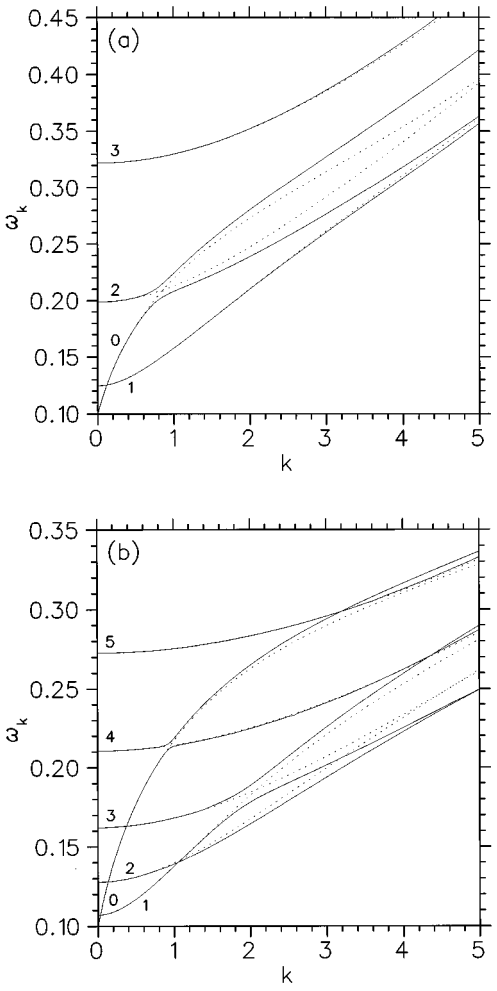

FIG. 1. Exact (solid lines) and approximate (dotted lines) dispersion relations for $\omega_H=1.1$ and (a) $l^2=0.0025$, (b) $l^2=0.007$. The numbers denote mode indices.

$$\beta_0=\frac{1}{2}\left(1-\frac{1-e^{-k}}{k}\right)=\frac{k}{4}+\mathcal{O}(k^2) \tag{22a}$$

and

$$\beta_{N\neq 0}=\frac{k^2}{2(k^2+N^2\pi^2)}-\frac{k^3[1-(-1)^N e^{-k}]}{(k^2+N^2\pi^2)^2}. \tag{22b}$$

This approximation of ψ inserted into (16) leads to the eigenfrequency

$$\omega_k^{(N)}=\sqrt{\alpha_N^2-\beta_N^2} \tag{23}$$

with

$$\alpha_N=\omega_H-1+l^2(k^2+N^2\pi^2)+\beta_N. \tag{24}$$

Since $\beta_0=\mathcal{O}(k)$ we get

$$\omega_k^{(0)}=\omega_H-1+\frac{k}{4}+\mathcal{O}(k^2). \tag{25}$$

This nodeless mode is the *dipolar mode* because in leading order of k the dipolar interaction dominates. The other modes (i.e., $N>0$) are ferromagnetic spin waves where the exchange interaction and the dipolar interaction are equally

important. For $k\to\infty$ we get the well-known bulk dispersion relation because $2\beta_N\to k^2/(k^2+N^2\pi^2)$.

Figure 1 shows a very good agreement between the exact dispersion relation and the approximate one. Of course the approximation cannot reproduce the hybridization because the ansatz (19) assumes independent branches. In the exact spectra crossings between two even modes or two odd modes are avoided by hybridization.[26,27] But crossings between even and odd nodes are possible because they belong to different irreducible representations of the inversion group. The size of the hybridization region increases with decreasing film thickness (i.e., increasing l).

B. Linear stability analysis

In order to analyze the stability of the ground state we have to discuss the eigenvalues of (16) with finite damping (i.e., $g\neq 0$) and finite driving (i.e., $\omega_h\neq 0$). The sign of the real part of $\lambda(k)$ decides whether the trivial solution is stable (negative sign) or unstable (positive sign) against a particular mode with wave number k. The value of ω_h where the real part of λ is exactly zero defines the instability threshold above which this particular mode will grow exponentially. This threshold is called the *neutral curve* $\omega_{h\mathrm{NC}}(k)$. In the case of parametric resonance it has local minima at values of k where the parametric resonance condition $\omega_k\approx n\omega/2$, n integer, is fulfilled.[1] The lowest minimum belongs to the first-order parametric resonance (i.e., $\omega_k\approx\omega/2$). The ground state is only stable if the real parts of λ of *all* modes are less than zero. The instability threshold ω_{hc} is therefore given by the absolute minimum of the neutral curve, i.e., $\omega_{hc}=\min_k\omega_{h\mathrm{NC}}(k)$. Thus the parametric resonance causing instabilities is always of first order.[28]

Based on the approximation (19) made in Sec. III. A we are able to calculate approximatively the neutral curve. In accordance with the Floquet theory we make the ansatz

$$(\mu_0,\mu_0^*)=(\mu_+,\mu_-)e^{i\omega t/2}+(\mu_-^*,\mu_+^*)e^{-i\omega t/2}. \quad (26)$$

This ansatz together with (20) is put into (16a) and (16b). We calculate the neutral curve directly by setting $\lambda=0$ in (16a) and (16b). This leads to a generalized eigenvalue problem with ω_h as the eigenvalue. The characteristic polynomial can be solved because it is quadratic in ω_h^2 (for details see Appendix B). The minimum of the neutral curve $\omega_{h\mathrm{NC}}^{(N)}$ in leading order of g is

$$\omega_{hc}^{(N)}=g\omega\sqrt{1+\frac{\omega^2}{4\beta_N^2}} \quad (27)$$

and takes place at $\omega_k^{(n)}=\omega/2+\mathcal{O}(g^2)$. It can be shown that $\omega_{hc}^{(N)}<\omega_{hc}^{(N+1)}$. Thus the dipolar mode (i.e., $N=0$) causes the instability. This result is consistent with the bulk calculation which leads to an instability of spin waves propagating perpendicular to the static field.[22]

The numerical approach to calculate the neutral curve is based on an extension of the approximations (19) and (26). We make the ansatz

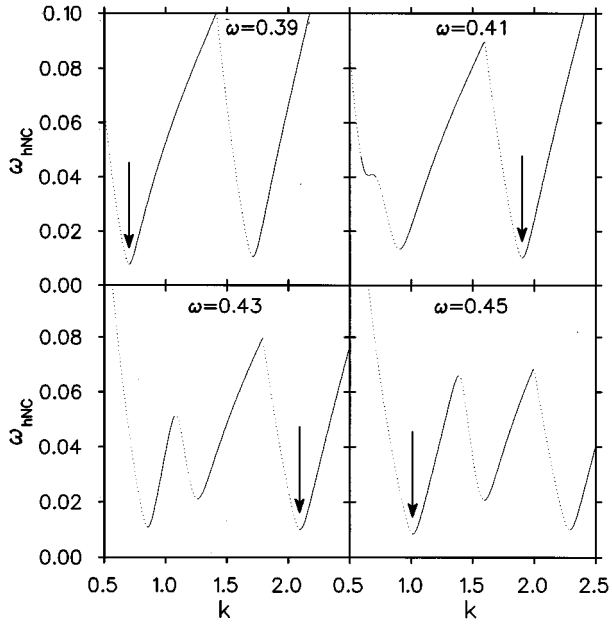

FIG. 2. Neutral curves for several values of ω around the hybridization point in Fig. 1(a). Parameters: $\omega_H=1.1$, $l^2=0.0025$, $g=0.01$, $N=4$, and $L=2$. An arrow denotes the absolute minimum of the neutral curve; it defines the instability threshold ω_{hc} and the critical wave number k_c. Solid (dotted) lines indicate points on the neutral curve where spatially periodic solutions with wavelength $2\pi/k$ bifurcate super(sub)critically.

$$\begin{pmatrix}\mu\\ \mu^*\end{pmatrix}=\sum_{n=0}^{N}\sum_{l=1}^{2L}\begin{pmatrix}\mu_{2l-2L-1,n}\\ \mu_{2l-2L-1,n}^*\end{pmatrix}e^{i(l-L-1/2)\omega t}\cos(n\pi z). \quad (28)$$

The exact solution of (16) fits also into this ansatz but with $N=L=\infty$. Thus L and N define numerical cutoffs in t and z, respectively, and (28) is therefore a Galerkin ansatz.[15] Again ψ is eliminated by (18). After projecting (16a) and (16b) onto $e^{i(l-L)\omega t}\cos(n\pi z)$ we get a homogeneous system of $4L(N+1)$ linear algebraic equations for $4L(N+1)$ unknown coefficients $\mu_{2l-2L-1,n}$ and $\mu_{2l-2L-1,n}^*$. Because (16) is linear in ω_h, it is a generalized linear eigensystem where ω_h is the eigenvalue. The characteristic polynomial is a polynomial of order $2L(N+1)$ in ω_h^2 because of symmetry. The neutral curve $\omega_{h\mathrm{NC}}$ is given by the smallest positive solution of this polynomial. I have solved this generalized eigensystem with a standard routine from the EISPACK subroutine package. It also yields the eigensolution (μ,μ^*,ψ) which is the starting point for the derivation of the amplitude equations in Sec. IV.

Figure 2 depicts several numerically obtained neutral curves. Each relative minimum is related to the first-order parametric resonance of a particular mode. For decreasing damping g the minima get closer to zero and become sharper. The distance to zero (i.e., the threshold) scales like g whereas the curvature scales like $1/g^2$.

The ω dependence of the relative minima of the neutral curve is shown in Fig. 3. The left-hand part of the figure looks almost identical to Fig. 1(a) because the deviation from the parametric resonance condition $\omega=2\omega_k$ is of order g^2.

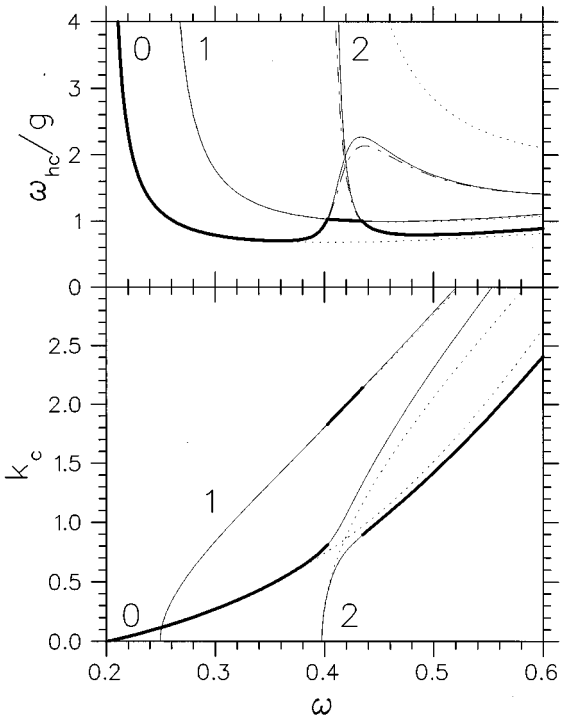

FIG. 3. Instability threshold ω_{hc} and critical wave number k_c as functions of ω. Parameters: $\omega_H=1.1$, $l^2=0.0025$, $N=4$, and $L=2$. Solid and dashed-dotted lines denote numerical values for $g=0.001$ and $g=0.01$, respectively. Dotted lines denote approximate values. Bold lines denote the absolute minimum. The numbers distinguish different modes.

The right-hand part of Fig. 3 shows the thresholds. The analytically obtained approximations are remarkable good except near the hybridization area. Here the threshold increases strongly. Therefore another mode becomes the most unstable one (usually the mode number one). The width of the interval in ω where this is the case is roughly *independent* of the damping constant g (see Fig. 3). At those values of ω where k_c switches from one mode to another a competition takes place between two different instabilities. Such a point is called a *codimension 2* point because it is defined by two parameters of the system (here ω_h and ω). All this does not happen when the damping constant g is too large or the coupling strength of the hybridized modes too low. There will be no codimension-2 bifurcation either due to the competition between the hybridized modes or between an additional mode. For example, the hybridization between the dipolar mode and the second exchange mode in Fig. 1(b) is too weak in order to change the qualitative behavior near this point. There is only a very small and tiny peak in the threshold $\omega_{hc}(\omega)$.

In the next section we derive the system of amplitude equations governing the dynamics of the amplitude of the most unstable modes. We do this only for the dipolar modes which are the most unstable modes outside of hybridization regions. The case near hybridization points will be treated separately in a forthcoming paper.

IV. DERIVATION OF THE SYSTEM OF AMPLITUDE EQUATIONS

In this section we describe in some detail how amplitude equations can be derived in principle and how it is done numerically.

The basic equations of motion (7) and (10) and the boundary conditions (12) can be written in symbolic form as

$$F(\mathbf{u},\omega_h)=0 \quad \text{and} \quad B(\mathbf{u})=0, \tag{29}$$

respectively, where of the pump field ω_h is the *control parameter*, and

$$\mathbf{u}(\mathbf{r},t)\equiv\begin{pmatrix} m(\mathbf{r},t) \\ m^*(\mathbf{r},t) \\ \phi_M(\mathbf{r},t) \end{pmatrix} \tag{30}$$

is the *order parameter* which contains the magnetization described by m and m^* and the magnetostatic potential ϕ_M.

From the previous section we know that the ground state (13) becomes unstable at $\omega_h=\omega_{hc}$. Above the instability threshold the *amplitudes* of the modes responsible for the instability increase exponentially. The nonlinearities of the equations of motion may eventually stop this growth. From bifurcation theory it is expected that for $\omega_h\to\omega_{hc}$ the values of the saturated amplitudes go to zero.[29] In order to calculate nontrivial solutions it is therefore natural to use a perturbation theory with $\omega_h-\omega_{hc}$ as the smallness parameter. The perturbation theory we use is a *multiple-scale perturbation theory*.[15,30] Instead of $\omega_h-\omega_{hc}$ it is more convenient to introduce a formal smallness parameter η which loosely speaking is proportional to the amplitudes and which will be set to one after the calculation. The order parameter as well as the control parameter are expanded into power series of η:

$$\omega_h=\omega_{h\mathrm{NC}}(k)+\omega_{h1}\eta+\omega_{h2}\eta^2+\mathcal{O}(\eta^3), \tag{31a}$$

$$\mathbf{u}=\mathbf{u}^T+\mathbf{u}_1\eta+\mathbf{u}_2\eta^2+\mathcal{O}(\eta^3), \tag{31b}$$

where $\mathbf{u}^T$ denotes the ground state (13). A multiple-scale perturbation theory assumes that the amplitudes of the destabilized modes vary slowly in time. It leads to a system of equations of motion for these amplitudes called *amplitude equations* or *Landau equations*. The latter name comes from the similarity to Landau's phenomenological theory of phase transition. In the language of bifurcation theory these equations are normal forms.

We have expanded ω_h around $\omega_{h\mathrm{NC}}(k)$ (i.e., the neutral curve at an arbitrary value of k) instead of ω_{hc} which is only a special case (i.e., the minimum of the neutral curve). This means that we calculate the bifurcation of a spatially periodic solutions from an arbitrary point on the neutral curve. After that we will restrict ourselves to the physically relevant case $k=k_c$ (i.e., the absolute minimum of the neutral curve).

Inserting the expansion (31) into the equation of motion (29) and sorting out powers of η we get a hierarchy of linear equations and linear boundary conditions,

$$\mathcal{L}[\mathbf{u}_n]=\mathbf{f}_n, \quad \mathcal{K}[\mathbf{u}_n]=\mathbf{b}_n \quad \text{for} \quad n=1,2,\ldots, \tag{32}$$

with $\mathbf{f}_1=\mathbf{b}_1=0$. The operators $\mathcal{L}$ and $\mathcal{K}$ are defined by the linearized equation of motion (14) for $\omega_h=\omega_{h\mathrm{NC}}$ and by the boundary conditions (12), respectively. The inhomogeneities $\mathbf{f}_n$ and $\mathbf{b}_n$ depend on the solutions $\mathbf{u}^T$, $\mathbf{u}_1,\ldots,\mathbf{u}_{n-1}$. Here $\mathbf{b}_n\equiv 0$ because the boundary conditions (12) are linear. In the case of (partially) pinned surface spins, the boundary conditions are nonlinear and $\mathbf{b}_n\neq 0$.

Since the first equation in this hierarchy is (14), the general solution is a linear combination of wave solutions (15) propagating in different directions

$$\mathbf{u}_1(\mathbf{r},t)=\begin{pmatrix} \sum_j e^{i\alpha_j}[A_j(T_n)e^{i\mathbf{k}_j\mathbf{r}}+\text{c.c.}]\mu(z,t) \\ \sum_j e^{-i\alpha_j}[A_j(T_n)e^{i\mathbf{k}_j\mathbf{r}}+\text{c.c.}]\mu^*(z,t) \\ \frac{2}{k}\sum_j [iA_j(T_n)e^{i\mathbf{k}_j\mathbf{r}}+\text{c.c.}]\psi(z,t) \end{pmatrix}, \tag{33}$$

where

$$\mathbf{k}_j=k(\cos\alpha_j\cdot\mathbf{e}_x+\sin\alpha_j\cdot\mathbf{e}_y), \tag{34}$$

$$T_n=\eta^n t,\quad n=1,2,\ldots, \tag{35}$$

and where μ, μ^*, and ψ are solutions of (16) for $\lambda=0$ and $\omega_h=\omega_{h\mathrm{NC}}(k)$. Note, that the amplitudes of counterpropagating waves cannot be chosen arbitrarily because the magnetostatic potential (i.e., the third component of $\mathbf{u}$) has to be real. The solution (33) excludes all waves which are either damped or growing on a time scale of order η^0. In the language of bifurcation theory this means that we only want to know what happens on the center manifold.

The amplitudes A_j are assumed to depend slowly on time. This is described by several time scales which are proportional to inverse powers of the smallness parameter η. The slow time dependence is formally established by introducing new independent time variables T_n and by the replacement

$$\partial_t\to\partial_t+\sum_{n=1}^{\infty}\eta^n\partial_{T_n}. \tag{36}$$

This leads to additional terms in the inhomogeneities $\mathbf{f}_n$ which are proportional to time derivatives on slow scales.

In order to get nontrivial solutions of (32) the inhomogeneities have to fulfill a solvability condition because $\mathcal{L}$ is a singular operator. For that reason we introduce the scalar product

$$\langle\mathbf{u}_a|\mathbf{u}_b\rangle=\int\int(m_a m_b+m_a^* m_b^*+\phi_a\phi_b)d^3r\,dt. \tag{37}$$

We define a adjoint operator $\mathcal{L}^\dagger$ by $\langle\mathbf{u}_a|\mathcal{L}\mathbf{u}_b\rangle\equiv\langle\mathcal{L}^\dagger\mathbf{u}_a|\mathbf{u}_b\rangle$. The boundary condition $\mathcal{K}\mathbf{u}=0$ is in our case self-adjoint. The solutions $\mathbf{u}^\dagger$ of the adjoint problem can be obtained from the solution (15) of the orginal problem by the transformation $(y,t,m)\to(-y,-t,(g-i)m/2)$, i.e.,

$$\mathbf{u}_j^\dagger(\mathbf{r},t)=\begin{pmatrix} \frac{e^{-i\alpha_j}\mu(z,-t)}{i-g} \\ \frac{e^{i\alpha_j}\mu^*(z,-t)}{-i-g} \\ \frac{i\psi(z,-t)}{k} \end{pmatrix} e^{-i\mathbf{k}_j\mathbf{r}}. \tag{38}$$

The solvability conditions read

$$\langle\mathbf{u}^\dagger|\mathbf{f}_n\rangle=0,\quad n=2,3,\ldots. \tag{39}$$

It means that *resonant terms* should be zero. The inhomogeneities are build up from superpositions of terms of the form $c(z,t)\exp(i\Sigma_{\nu=1}^n\mathbf{k}_{j_\nu}\mathbf{r})$. A term is resonant if $|\Sigma_{\nu=1}^n\mathbf{k}_{j_\nu}|=k$.

All inhomogeneities have two terms which are linear in the amplitudes A_j

$$\mathbf{f}_{n+1}=\omega_{hn}\cos\omega t\begin{pmatrix}(i-g)m_1\\(-i-g)m_1^*\\0\end{pmatrix}-\partial_{T_n}\begin{pmatrix}m_1\\m_1^*\\0\end{pmatrix}+\mathcal{O}(A^2),$$

$$n=1,2,\ldots.$$

After the projection onto $\mathbf{u}_j^\dagger$ we get

$$S_t\partial_{T_n}A_j=\omega_{hn}S_hA_j+\mathcal{O}(A^2) \tag{40}$$

with

$$S_t=\int_0^1\int_0^{2\pi/\omega}\left(\frac{\mu(z,-t)\mu(z,t)}{i-g}+\text{c.c.}\right)dt\,dz \tag{41}$$

and

$$S_h=\int_0^1\int_0^{2\pi/\omega}[\mu(z,-t)\mu(z,t)\cos\omega t+\text{c.c.}]dt\,dz. \tag{42}$$

Because of (36) and (31a) the sum over all equations (40) multiplied by η^n yields

$$S_t\dot{A}_j=(\omega_h-\omega_{h\mathrm{NC}})S_hA_j+\mathcal{O}(A^2). \tag{43}$$

It is convenient to introduce the dimensionless control parameter,

$$\epsilon\equiv\frac{\omega_h-\omega_{h\mathrm{NC}}}{\omega_{h\,\mathrm{NC}}}=\frac{h-h_{\mathrm{NC}}}{h_{\mathrm{NC}}}. \tag{44}$$

It is negative (positive) below (above) the threshold. After dividing (43) by $\omega_{h\mathrm{NC}}S_h$ we get the linear part of the amplitude equations

$$\tau_0\dot{A}_j=\epsilon A_j+\mathcal{O}(A^2), \tag{45}$$

with

$$\tau_0=\frac{S_t}{\omega_{h\mathrm{NC}}S_h}. \tag{46}$$

The characteristic time scale of the dynamics of the spin-wave amplitudes are given by τ_0/ϵ. It diverges at the threshold because of $\epsilon\to 0$. This is the well-known critical slowing-down at nonequilibrium phase transitions. For the

approximation introduced in Sec. III we can calculate τ_0 analytically. Using the results from Appendix B we get for the dipolar mode

$$\tau_0=\frac{1}{\alpha_0 g}+\mathcal{O}(g^0), \tag{47}$$

where α_0 is defined by (24). Thus the time scale is, as expected, proportional to the inverse of the damping constant g.

In order to get the nonlinear terms of (45) we first look at the quadratic term of $\mathbf{f}_2$. It reads

$$-\begin{pmatrix}(i-g)m_1\partial_z\phi_1\\(-i-g)m_1^*\partial_z\phi_1\\2\partial_z[|m_1|^2B(z)]\end{pmatrix}, \tag{48}$$

where $B(z)$ is the box function (11). The projection of this term onto the adjoint solution (38) leads to the quadratic term in (45). From Sec. III we know that the modes are either even or odd in the z direction. Therefore (48) is always odd. From this it follows that *the quadratic term in the amplitude equations is absent for even modes* because the adjoint mode is also even and the projection is therefore zero.

Usually a quadratic term is absent since the most unstable mode is the dipolar mode which is even. Only near hybridization points where an odd mode becomes the most unstable one do we get a quadratic term. The dipolar mode is even because we have assumed that the sample is symmetric under reflection at the plane $z=1/2$. In a real sample this symmetry is often broken because the film is usually mounted on a substrate which may have a different permeability than the air above the film. Furthermore the substrate may change the boundary conditions for the magnetization. In the following we assume that the quadratic term is absent. The more general case will be treated in a forthcoming paper.

In order to calculate $\mathbf{f}_3$ we need the solution of (32) for $n=2$. A general solution is the sum of a particular solution and a solution of the homogeneous equation. The relevant part of the latter one (i.e., the part on the center manifold) is (33) where the amplitudes A_j are replaced by some other amplitudes. We omit this part because it leads only to a renormalization of the amplitudes A_j. From the quadratic part (48) of the inhomogeneity $\mathbf{f}_2$ we get terms like $\mathbf{c}(z,t)A_jA_{j'}\exp[i(\mathbf{k}_j+\mathbf{k}_{j'})\mathbf{r}]$ which lead to similar terms in the solution $\mathbf{u}_2$. Actually the inhomogeneous version of (16) should be solved for $\lambda=0$ and $k=|\mathbf{k}_j+\mathbf{k}_{j'}|$. We do this numerically by the Galerkin ansatz (28) where ψ has been eliminated by (18). The nonlinear terms in $\mathbf{f}_3$ have the same parity as the adjoint solution $\mathbf{u}_j^\dagger$. Thus the solvability condition leads always to a nonzero third-order term in the amplitude equations (45).

What is the general structure of this third-order term? We can answer this question by looking at the possible resonances of $\mathbf{f}_3$ for k_j. Since the nonlinear terms of $\mathbf{f}_3$ are of the form $\mathbf{c}(z,t)A_jA_{j'}A_{j''}\exp[i(\mathbf{k}_j+\mathbf{k}_{j'}+\mathbf{k}_{j''})\mathbf{r}]$, nine different combinations are possible (see Fig. 4). Note that the amplitude which belongs to $-\mathbf{k}_j$ is A_j^*. Three combinations lead to a term of the form $|A_j|^2A_j$ whereas six combinations lead to a term of the form $|A_{j'}|^2A_j$ with $j'\neq j$. Thus the amplitude equations up to third order read

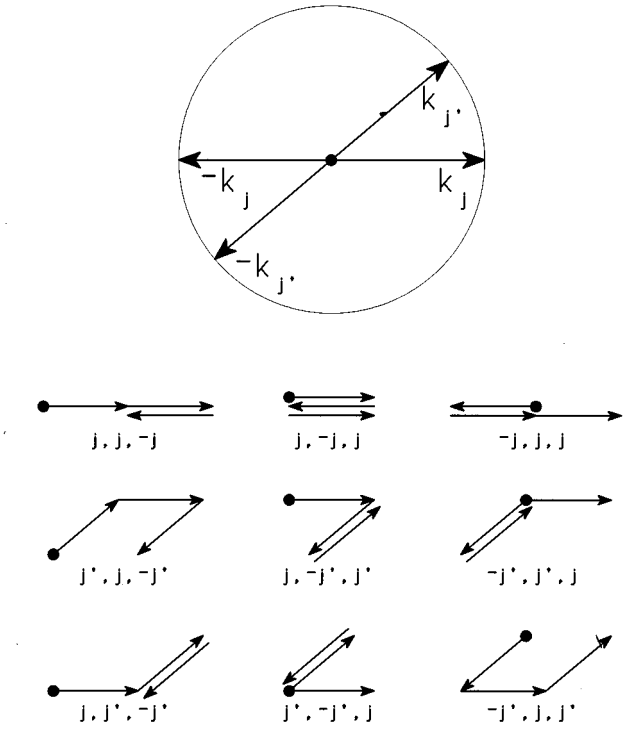

FIG. 4. All possible resonances which contributes to the third-order term in the amplitude equation for A_j. The notation, j_1,j_2,j_3 means the resonance $\mathbf{k}_{j_1}+\mathbf{k}_{j_2}+\mathbf{k}_{j_3}$.

$$\tau_0\dot{A}_j=\epsilon A_j-c\left[|A_j|^2+\sum_{j'\neq j}a(\alpha_j-\alpha_{j'})|A_{j'}|^2\right]A_j. \tag{49}$$

It can be shown that the coefficients of the nonlinear terms are real. The *coupling function* $a(\alpha)$ has the following properties:

$$a(\alpha\to 0)=2,\quad a(\alpha+\pi)=a(\alpha),\quad a(-\alpha)\neq a(\alpha). \tag{50}$$

The first property is caused by the fact that, e.g., the resonances $(j',j,-j')$ and $(j,j',-j')$ give the same contributions as $(j,j,-j)$ if $\mathbf{k}_{j'}\to\mathbf{k}_j$ (see Fig. 4). The rotational symmetry is responsible for the second property.[31] The last property is caused by the fact that the *dipolar* field strongly breaks the reflection symmetry at any plane perpendicular to the film plane.

The broken reflection symmetry has strong consequences. In order to see this we assume for a moment that it is not broken which yields an even coupling function $a(\alpha)$. In this case the system of amplitude equations (49) can be written in a variational form

$$\tau_0\dot{A}_j=-\frac{\partial L}{\partial A_j^*}, \tag{51}$$

where

$$L=\sum_j\left[-\epsilon|A_j|^2+\frac{c}{2}|A_j|^4+\frac{c}{2}\sum_{j'\neq j}a(\alpha_j-\alpha_{j'})|A_{j'}A_j|^2\right] \tag{52}$$

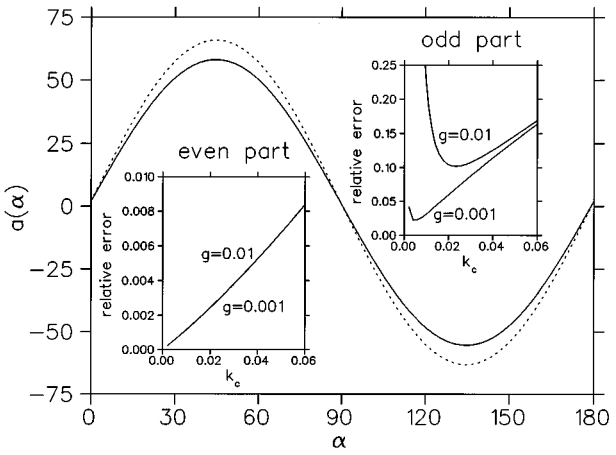

FIG. 5. The coupling function $a(\alpha)$ for $\omega_H=1.1$, $l^2=0.0025$, $\omega=0.22$, and $g=0.001$. The solid line is the numerical result for $N=4$, $L=2$ whereas the dashed line is the analytical result (54) with a_s given by (55). The insets depict the maximum of the relative deviation of the numerical result from the analytical result.

is a real function called *Lyapunov function*. It corresponds to the free energy in Landau's phenomenological theory of phase transitions. It *decreases monotonically* in time if the amplitudes are solutions of (51). Thus limit cycles or irregular oscillations are not possible for $t\to\infty$. In systems like the Faraday instability or the Rayleigh-Bénard convection where the reflection symmetry is not broken, Eq. (51) describes therefore only stationary attractors. In our case the reflection symmetry is broken, and the coupling function is not even. In fact the odd part of $a(\alpha)$ (i.e., $[a(\alpha)+a(-\alpha)]/2$) is usually quite large (see Fig. 5). A Lyapunov function does not exist. Therefore limit cycles or even chaotic motions are possible at the onset of the main instability. In Sec. VI we will see that this is indeed the case.

The calculation of τ_0, b, c, and $a(\alpha)$ is in general possible only numerically. The algorithm I have used is based on the fact that all functions which are involved in the calculation have the general form

$$F(\mathbf{r},t)=\sum_j A_+^{n_j^+}A_-^{n_j^-}c_j\exp\left[i\left(n_j^+\mathbf{k}_+\mathbf{r}+n_j^-\mathbf{k}_-\mathbf{r}+n_j^z\pi z+n_j^t\frac{\omega}{2}t\right)+n_j^\phi|n_j^+\mathbf{k}_++n_j^-\mathbf{k}_-|z\right], \tag{53}$$

where $\mathbf{k}_\pm=k(\cos(\alpha/2)\cdot\mathbf{e}_x\pm\sin(\alpha/2)\cdot\mathbf{e}_y)$, all n's are integer, c_j is a complex number, and $A_\pm^{-n}\equiv(-A_\pm^*)^n$. The terms with $n_j^\phi\neq0$ are necessary to describe parts of the magnetostatic potential which are obtained from exact integration (18). It is easy to write subroutines for such an integration and other operations (multiplication, addition, scalar product, etc.) in the function space defined by (53). In order to construct the solution $\mathbf{u}_2$ four linear algebraic equations have to be solved which I have done by using a standard routine from the LINPACK subroutine package.

Of special importance is the coupling function $a(\alpha)$. As we will see in the next section, the functional dependence of a on α tells us which patterns exist and which of them are stable. In the limit $k_c\to0$ we can derive the functional form of a analytically because the dipolar mode becomes uniform in the z direction (see Appendix C):

$$a(\alpha)=\frac{4}{3}+\frac{2}{3}\cos 2\alpha+a_s\sin 2\alpha, \tag{54}$$

where a_s is given by (C5). It can be calculated in general only numerically. But for $g\to0$ it is possible to do this analytically because the Galerkin ansatz (28) for $L=1$ becomes exact. We get

$$a_s=\frac{k_c}{3\omega g}. \tag{55}$$

Thus, in leading order of g the coupling function is an odd function which reflects the strongly broken reflection symmetry. Nevertheless the even part of the coupling function, although of higher order, will be important for the saturation of the amplitude of the unstable spin waves.

Figure 5 shows a comparison between analytic and numerical results for small values of k_c. The even part of $a(\alpha)$ is quite well approximated by $(4+2\cos2\alpha)/3$. The error is not larger than one percent and is independent of g. The deviations in the odd part of the coupling function are at least by a factor of 10 larger, and they strongly depend on g.

The next order of the amplitude equations can be calculated in principle, but it would be an extremely tedious task to do that. This is especially true for even modes where the next term is of fifth order because the fourth-order term is absent for the same reason as for the quadratic term (i.e., $\mathbf{f}_4$ is always odd in z).

Higher-order terms are important if c (i.e., the overall strength of the third-order terms) becomes small or negative. Numerical calculations show that c changes its sign near the minima of the neutral curve (see Fig. 2). At the minimum c is always positive except near hybridization points. But the point on the neutral curve where c is equal to zero approaches the minimum for $g\to0$. This behavior is typical for parametric resonance because the resonance frequency usually depends on the amplitude which leads to a foldover of the resonance line.[32] In our case the demagnetizing field is responsible for this frequency detuning.[33]

V. STATIONARY SOLUTIONS OF THE AMPLITUDE EQUATIONS

In this section we investigate stationary patterns of (49) and their stability. The general stationary pattern, called the N-wave pattern, is built up from N different standing waves, i.e., N amplitudes A_j are unequal zero whereas the rest is zero.

It is more convenient to replace the amplitudes in (49) by

$$A_j=R_je^{i\chi_j}, \tag{56}$$

which leads to

$$\tau_0 \dot{R}_j = \epsilon R_j - c\left[R_j^2 + \sum_{j' \neq j} a(\alpha_j - \alpha_{j'}) R_{j'}^2\right] R_j, \qquad (57)$$

$$\tau_0 R_j \dot{\chi}_j = 0. \qquad (58)$$

Thus $\chi_j = \text{const}$ for all waves. Two linear combinations of χ_j are related to the translation symmetry in the (x,y) plane. Assuming $\epsilon, c > 0$ and introducing the scaling

$$t \to \frac{\tau_0}{2\epsilon} t, \text{ and } P_j = \frac{c}{\epsilon} R_j^2, \qquad (59)$$

we get

$$\dot{P}_j = \left[1 - P_j - \sum_{j' \neq j} a(\alpha_j - \alpha_{j'}) P_{j'}\right] P_j. \qquad (60)$$

Equation (60) does not contain the control parameter ϵ any more. This fact has the important consequence that *the dynamical behavior of the solutions is independent of the strength of the control parameter*. The control parameter only determines the time scale on which the dynamics happens. Thus it is not possible to describe secondary instabilities in the framework of a third-order amplitude equations without quadratic terms. The dynamics is only determined by the coupling function $a(\alpha)$.

For a given set of angles $\{\alpha_1, \ldots, \alpha_N\}$ the stationary N-wave pattern is uniquely given because it is determined by a system of linear algebraic equations. But the solution does not make sense for all possible angles because all P_j's have to be positive. Nevertheless solutions exist for a finite number of connected subsets in the angle space.

In order to investigate the stability of the stationary solutions we linearize (60) around the solution. This leads to an equation of motion for small perturbations δP_j which can be solved by the ansatz $\delta P_j = C_j e^{\lambda t}$. We get an eigenvalue problem which separates into the nontrivial case

$$(P_j + \lambda) C_j + P_j \sum_{j' \neq j} a(\alpha_j - \alpha_{j'}) C_{j'} = 0, \quad j = 1, \ldots, N, \qquad (61)$$

and into infinitely many trivial cases where we immediately get

$$\lambda(\alpha) = 1 - \sum_{j=1}^{N} a(\alpha - \alpha_j) P_j, \quad \alpha \notin \{\alpha_1, \ldots, \alpha_N\}. \qquad (62)$$

We define two kinds of stability.

Internal stability: A pattern will be internally stable if the real parts of all eigenvalues λ of the nontrivial case (61) are less than zero. Thus a perturbation of the amplitudes which build the pattern decays to zero.

External stability: A pattern will be externally stable if $\lambda(\alpha)$ defined by (62) is less than zero for all α. External stability means that the amplitudes which do not build the pattern do not grow.

A pattern is stable if it is externally as well as internally stable. If a pattern is externally unstable there will be at least one interval of α for which $\lambda(\alpha)$ is positive. Figure 6 shows $\lambda(\alpha)$ for several types of N-wave patterns. Using (60) and (50) we get

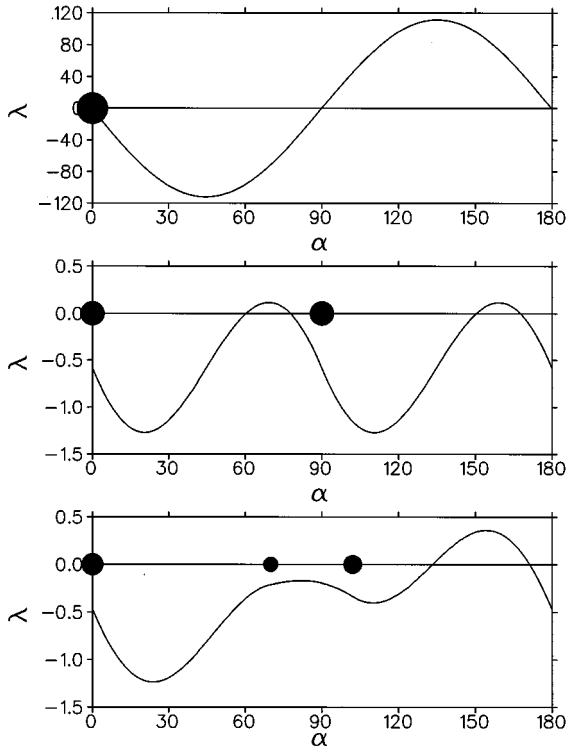

FIG. 6. Examples of external instability. Parameters: $\omega_H = 1.1$, $l^2 = 0.0025$, $g = 0.001$, $N = 4$, $L = 2$, $\omega = 0.25$ yielding $k_c = 0.117$. The nonvanishing amplitudes of a pattern are denoted by circles. The radius of a circle is proportional to the amplitude. The growth rate $\lambda(\alpha)$ defined by (62) is shown for a one-wave pattern, a square, and a three-wave pattern ($\alpha_2 = 70°$ and $\alpha_3 = 102°$).

$$\lambda(\alpha \to \alpha_j) = -P_j. \qquad (63)$$

Thus the pattern is externally stable against waves with angles from a finite interval around α_j. In the following we calculate N-wave patterns and their stability for different values of N.

A. One-wave patterns

The simplest pattern is built up from a single standing wave, i.e., $P_1 = 1$ and $P_{j \neq 1} = 0$. It is a stripe pattern similar to the roll pattern in Rayleigh-Bénard convection. From (61) we find immediately that one-wave patterns are always internally stable because $\lambda = -1$. They are externally stable if $\lambda(\alpha) = 1 - a(\alpha) < 0$ for all α. This is true only if the minimum of $a(\alpha)$ is larger than one. In the limit $k_c \to 0$ where the coupling function has the form (54), one-wave patterns are always unstable because $\lambda(\pi/2) = 1/3 > 0$. In the general case where $a(\alpha)$ can be calculated only numerically, I have always found that the minimum of coupling functions is strongly negative (see, e.g., Fig 5) due to the odd part of $a(\alpha)$. The angle of the fastest growing wave is roughly 45° behind the stripe pattern (see, e.g., Fig. 6).

This external instability of one-wave pattern is similar to the Küppers-Lortz instability in rotated Rayleigh-Bénard

convection.[12] This rotation breaks the reflection symmetry and leads therefore to an odd contribution for the coupling function $a(\alpha)$. But contrary to our situation the Küppers-Lortz instability can be controlled by the angular velocity. The odd part of the coupling function increases with the angular velocity. If a threshold is exceeded the roll pattern becomes unstable. The most unstable wave is roughly 60° ahead of the roll pattern.

B. Two-wave patterns

Two-wave patterns are built by two standing waves with amplitudes

$$P_{\pm}=\frac{1-a(\pm\Delta\alpha)}{1-a(\Delta\alpha)a(-\Delta\alpha)}, \quad \text{with } \Delta\alpha=\alpha_{+}-\alpha_{-}. \tag{64}$$

Since $P_{\pm}$ should be positive two-wave patterns exist only if either $a(\pm\Delta\alpha)<1$ and $a(\Delta\alpha)a(-\Delta\alpha)<1$ or $a(\pm\Delta\alpha)>1$. Thus they should always exist for $\Delta\alpha$ near zero because $a(0)=2$. For small values of the damping constant g the odd part of the coupling function a becomes very large. Therefore the signs of $a(\pm\Delta\alpha)-1$ are always different except for $\Delta\alpha$ near zero and near $\pi/2$. Because the odd part of a scales like $1/g$ the width of the interval of existence scales like g. Two-wave patterns around $\pi/2$ (i.e., squares) exist if $a(\pi/2)+1>0$ which is the case for $k_c\to 0$ since (54) holds. Nothing changes qualitatively in the general case where the coupling function can be calculated only numerically.

The analysis of the eigenvalue problem (61) leads to the condition for internal stability which reads $a(\Delta\alpha)a(-\Delta\alpha)<1$. Thus patterns for $\Delta\alpha$ near zero are always internally unstable. Squares are stable. This can be proved in the limit $k_c\to 0$ (see Appendix D). This seems to be true also in the general case.

In order to study the external stability of square patterns $\lambda(\alpha)$ defined by (62) has to be calculated. In the limit $k_c\to 0$ square patterns are stable (see Appendix D). But in the general case they become unstable if k_c exceeds some threshold. An example is shown in Fig. 6. Figure 7 shows that the threshold monotonically increases with the strength ω_H of the static field. It is roughly independent of the exchange length l which means that the instability is mainly caused by the dipolar interaction. On the other hand the threshold strongly depends on the damping constant g. It monotonically increases with g.

Also stable rhombic patterns exist. But their interval of $\Delta\alpha$ is around $\pi/2$. Its width scales with the damping constant g and is therefore very small. Thus stable rhombic patterns are practically indistinguishable from square patterns. Figure 8(a) shows how a square pattern looks if it appears in an experiment where Faraday rotation is used for visualization.

C. Three-wave patterns

First we discuss regular three-wave patterns, i.e., hexagons. Appendix D shows that for $k_c\to 0$ they exist, they are externally stable, but they are internally only marginally stable. That is, an oscillating mode with frequency $a_s/2$ exists which neither decays nor increases. From numerically calculated coupling functions I found that the correction terms to (54) are always such that hexagons are internally unstable contrary to what is stated in Ref. 11.[34] This is similar to what is found in a rotated Rayleigh-Bénard system.[13]

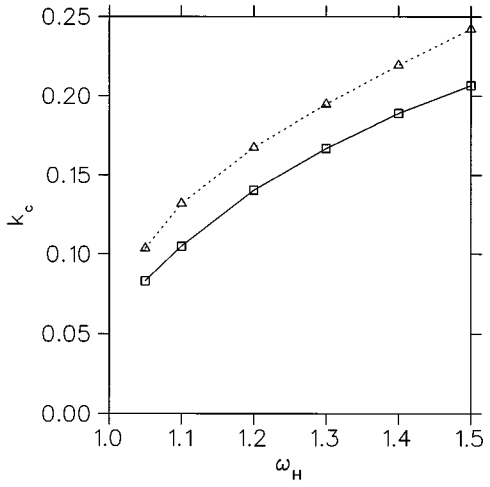

FIG. 7. Stability of squares and quasiperiodic three-wave patterns. For values of k_c above the solid (dotted) line squares (three-wave patterns) are unstable. The thresholds are calculated for $g=10^{-3}$ and $l^2=0.0025$. Quantitatively almost the same values are obtained for $l^2=0.0001$.

The general stationary three-wave pattern is defined by arbitrary angles α_j. Since the P_j's have to be positive, not all angles are allowed. In the limit $k_c\to 0$ and $g\to 0$ where the coupling function $a(\alpha)$ is given by (54) and where $a_s\to\infty$ the set of possible angles can be calculated analytically (see Appendix E). It turns out that any combination of angles has to be inside the region defined by

$$\alpha_2-\alpha_1, \quad \alpha_3-\alpha_1<90°<\alpha_3-\alpha_1. \tag{65}$$

Due to permutation symmetry and periodicity of $a(\alpha)$ additional angles are allowed. All allowed angle combinations can be most easily visualized by cutting the circle with three lines into six pieces. The lines should go through the center of the circle. They represent three pairs of wave vectors like in Fig. 4. The circle has to be cut in such a way that the angle of each wedge is less than 90°. For finite but large a_s the allowed region is inside the triangle defined by (65). The distance of the border to an edge of the triangle is of order $1/a_s^2$ whereas in the corners it is of order $1/a_s$. In the general case where k_c is arbitrary but g still small the same region of allowed angles has been found numerically.

Contrary to two-wave patterns where for small damping only squares are allowed a whole variety of three-wave patterns are possible. There is a dense set of periodic patterns. A pattern is periodic if integers n_1, n_2, and n_3 can be found with

$$n_1\mathbf{k}_1+n_2\mathbf{k}_2+n_3\mathbf{k}_3=0 \tag{66}$$

and with

$$n_1^2<n_2^2+n_3^2, \text{ and cycl. perm.} \tag{67}$$

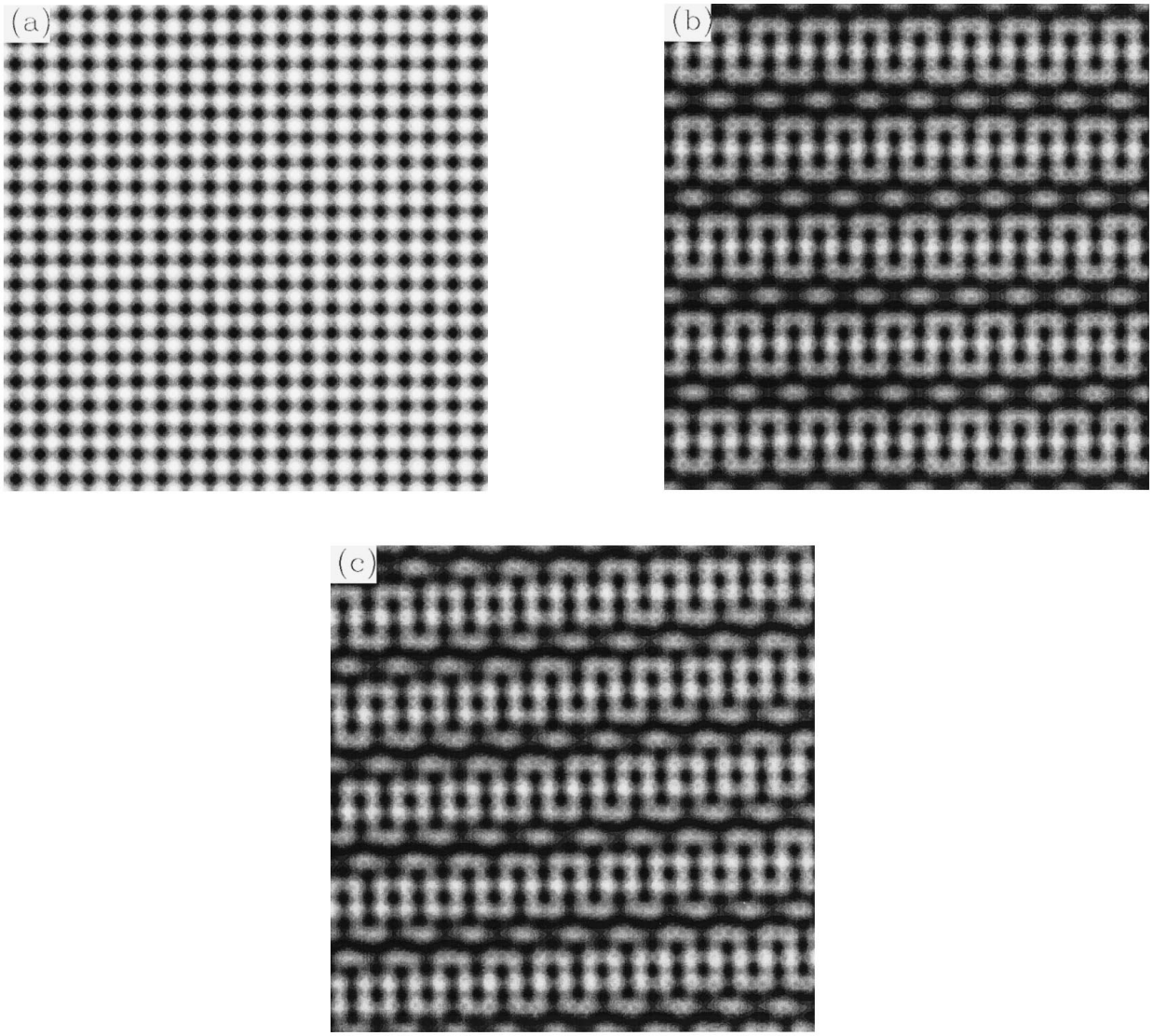

FIG. 8. Simulated photographs of a square pattern (a), a periodic (b) and a quasiperiodic (c) three-wave pattern assuming Faraday rotation as the appropriate visualization technique. Parameters: $\omega_H=1.1$, $l^2=0.0025$, $g=0.001$, $N=4$, $L=2$, $\omega=0.22$ (i.e. $k_c=0.043$), $\alpha_1=0°$, (a) $\alpha_2=90°$, (b) $\alpha_2=75.5225°$, $\alpha_3=104.4775°$, (c) $\alpha_2=70°$, $\alpha_3=100°$. The angles for the periodic three-wave pattern are chosen in such a way as to fulfill (66) for $n_1=1$ and $n_2=n_3=2$. The grey scale denotes the temporal average of $M_x^2+M_y^2$ where black means zero.

The last condition is a consequence of (65). Hexagons ($n_1=n_2=n_3$) are periodic patterns with the smallest unit cell. Quasiperiodic patterns are patterns for which (66) cannot be fulfilled for any set of integer. These are the generic three-wave patterns because the measure of periodic patterns is zero. In practice one cannot distinguish between periodic patterns with large unit cells and quasiperiodic patterns because of finite extension of the sample in lateral direction. Examples of a periodic and a quasiperiodic three-wave pattern are shown in Figs. 8(b) and 8(c), respectively.

All three-wave patterns are internally stable for $k_c\to 0$ and $g\to 0$ (see Appendix E). But numerical hexagons are unstable in this limit as already mentioned above. Figure 9 shows the regions of internal and external stability for three different values of k_c. We see that for small values of k_c indeed all patterns are internally stable except around $\alpha_2-\alpha_1=\alpha_3-\alpha_2=60°$. This instability region grows with increasing k_c. The region of external stability does not fill the whole existence triangle even in the limit $k_c\to 0$ and $g\to 0$ (see also Fig. 1 in Ref. 11). Thus there exist externally unstable patterns. The region of external stability shrinks with increasing k_c and eventually disappears. Above a certain critical value of k_c all possible three-wave patterns are either externally or internally unstable. Figure 7 shows that this threshold increases with the external static field ω_H. The threshold is always larger than the threshold of square patterns. Again it is nearly independent of the exchange length l and increases with the damping constant g.

D. *N*-wave patterns

Appendix D shows that regular N-wave patterns are externally unstable if N is larger than three. This is proved only in the limit $k_c\to 0$ where (54) holds but all numerically calculated coupling functions share this property. Furthermore,

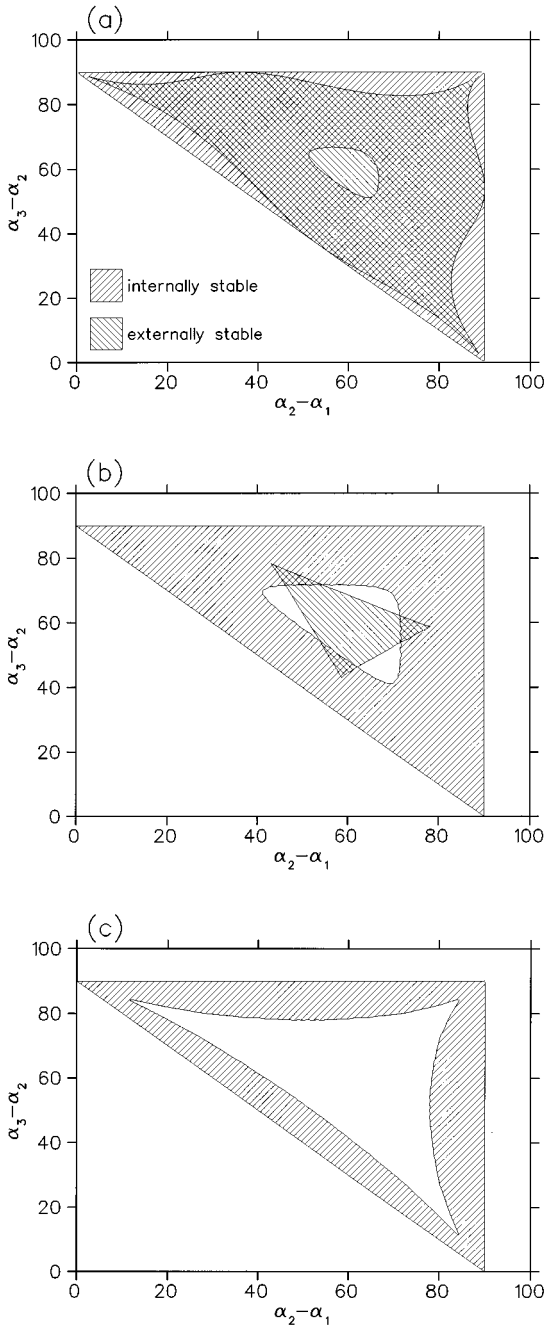

FIG. 9. Stability of three-wave patterns. Parameters: $\omega_H=1.1$, $l^2=0.0025$, $g=0.001$, $N=4$, and $L=2$. (a) $\omega=0.22$ yielding $k_c=0.043$, (b) $\omega=0.25$ yielding $k_c=0.117$. (c) $\omega=0.30$ yielding $k_c=0.272$.

in numerical simulations of the system of amplitude equations (49) I have never found internally stable N-wave patterns with $N>3$.

VI. TEMPORAL BEHAVIOR OF THE AMPLITUDE EQUATIONS

In the previous section we have seen that above the threshold not only one stable stationary pattern is possible but large continuous families of patterns (squares and three-wave patterns). This multistability is very common in pattern formation[1] and raises immediately the question *which pattern the system selects*. This question can be answered for thermal equilibrium systems where a free-energy functional exists. This is also possible for some models of systems far from thermal equilibrium where a Lyapunov functional exists which plays the role of a free energy. The absolute minimum of the free energy or of the Lyapunov functional gives the ground state. All relative minima define metastable states. On a large time scale which is determined by the barrier height and the strength of thermal noise the system will eventually select the ground state.

In Sec. IV we have seen that the system of amplitude equations (49) does not have a Lyapunov functional because the coupling function $a(\alpha)$ is not even. Thus regular and irregular oscillations may occur which lead to a richer temporal behavior than usual where the coupling is symmetric. On the other hand, the lack of a Lyapunov function makes it difficult to solve the problem of pattern selection.

In the previous section we have also seen that if k_c exceeds some threshold, all stationary patterns are unstable. In that case we want to know the temporal behavior of the system of amplitude equations.

Both questions can be attacked by numerical integration of the amplitude equations (57). By a rescaling similar to (59) we can set formally $\tau_0=\epsilon=c=1$. I have done this integration for a set of N equally distributed wave vectors (i.e., $\alpha_j=\pi j/N$) with $N=90$. The selected pattern may depend on the history of the system.[1] For that reason I have assumed that, like in most experiments, the pump field is suddenly tuned from below threshold to above threshold. This situation can be simulated by an initial condition with randomly chosen amplitudes with $0<R_j<0.01$. The dynamical behavior strongly depends on whether a noise term is added to the equations of motion or not.

A. Dynamics without noise

First I present the result of the simulations without noise. Figure 10 shows the typical behavior for three different values of k_c. Note that for each example the coupling function is the same as for the corresponding part of Fig. 9. For clarity, simulations with $N=36$ are shown instead of $N=90$, but the presented examples are typical for $N=90$.

The behavior at the initial stage (roughly up to 20 time units) is the same for all coupling functions. This is most clearly seen in Fig. 10(a) because the time scale is by a factor of 10 smaller than in Figs. 10(b) and 10(c). At the beginning all amplitudes grow exponentially because the nonlinear terms in (57) are small. When the amplitudes are large enough the nonlinearities lead to an intermediate saturation. After that, competition takes place, and only three amplitudes survive whereas all other amplitudes die out exponentially. Note that in general the surviving amplitudes do not coincide with those which are initially the largest ones. For example, at $t=0$ the three largest amplitudes in Fig. 10(a) are R_{16}, R_{30}, and R_{10} in that order.

After this initial stage of the dynamics, the further temporal behavior depends on the coupling function. In the case $k_c\to 0$ there is a large probability that the initially selected three-wave pattern is stable like in the example shown in Fig. 10(a). By repeating the numerical experiment I found that mostly three-wave patterns are selected. They are presum-

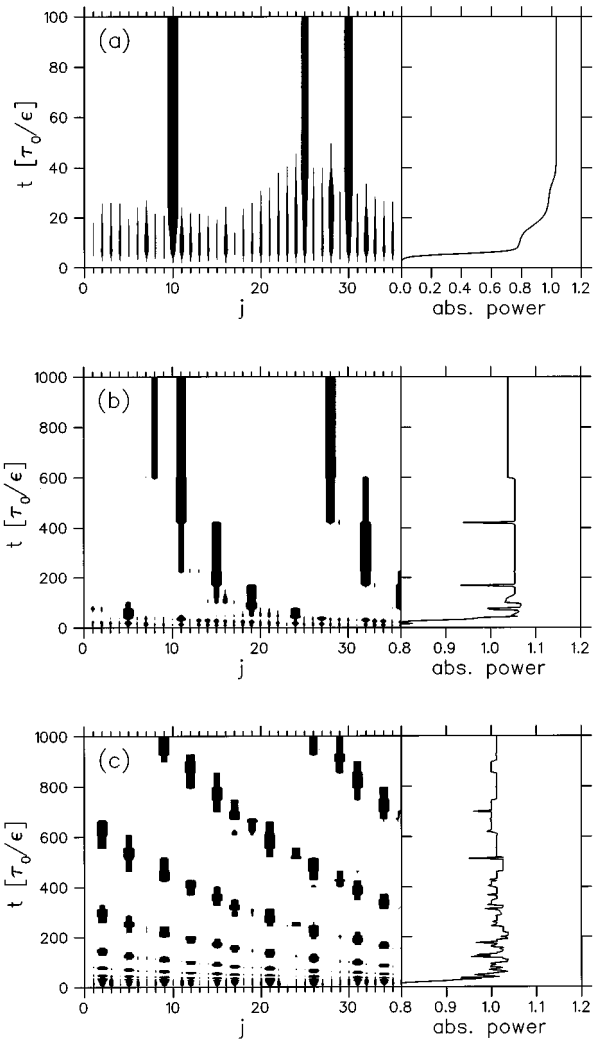

FIG. 10. The dynamical behavior of a system of 36 amplitude equations. The angles α_j are equally spaced. On the left-hand side, the absolute values of the amplitudes of the modes $j=1,\ldots,36$ are represented by the widths of the lines plotted against the vertical t axis. The right-hand side shows the absorbed power in units of the absorbed power of a one-wave pattern, which is given by $\Sigma_j P_j$. The parameters are the same as for Fig. 9.

ably distributed equally over the space of stable angle configurations. Squares occur very rarely because it is very unlikely that two amplitudes are selected with wave vectors forming an angle from the small stable interval around 90°. Since the width of this interval scales with the damping constant g, the probability for squares is presumably proportional to g. Below we will see that in the presence of noise the situation is reversed and squares are much more probable than three-wave patterns.

In Sec. V C we have seen that the region of stable three-wave patterns decreases for increasing k_c (see also Fig. 9). Thus the probability of the initially selected three-wave pattern to be stable also decreases. The typical behavior for that case is shown in Fig. 10(b). At the beginning one of the large number of *internally stable* three-wave patterns [see Fig. 9(b)] will be selected. But because it is externally unstable, amplitudes which have died out after the initial growth become unstable again and grow. Contrary to the initial stage the growth rate now depends on the angle. It is given by $\lambda(\alpha)$ defined by (62). The fastest growing amplitude eventually competes with the established amplitudes. Since four-wave patterns are internally unstable this competition has loosers which includes at least one of the established waves. Thus the system switches from one internally stable but externally unstable pattern to another one which is at least internally stable. Such *pattern switching* is mathematically speaking a *heteroclinic orbit* between two internally stable patterns.

In order to understand this pattern switching, we first discuss as the simplest example a system of three amplitude equations corresponding to three equally spaced angles. This system was investigated in ecology where it is a model for the competition of three species.[35] The internally stable solutions are one-wave patterns whereas the hexagon pattern is internally unstable. Starting with a slightly disturbed hexagon the solution winds outward on a spiral. It does not reach an ordinary limit cycle. Instead it approaches for $t\to\infty$ a sequence of heteroclinic orbits. Each of them is a switching from a one-wave pattern to another one-wave pattern rotated by 60°. Because the heteroclinic orbits are approached closer and closer, the waiting time between two switchings increases. This gives rise to an unusual type of limit cycle with a diverging period. Mathematically speaking this system of equations is structurally unstable which means that a tiny change in the equation of motion changes the behavior qualitatively. For example, the behavior is extremely sensitive to noise. Busse and Heikes have used the same system of amplitude equations for rotated Rayleigh-Bénard convection above the Küppers-Lortz instability.[13] From this sensitivity on noise they conclude that weak turbulence occurs right at the onset of convection.

The behavior of this simple system of three amplitude equations occurs qualitatively also in the general case. For example we clearly see in Fig. 10 an increase of the average waiting time. The situation is more complicated because there is a complex ''net'' of heteroclinic orbits which becomes denser and denser for an increasing number of amplitude equations. The nodes of this net are the internally stable N-wave patterns. Thus there are infinitely many. From each externally unstable node heteroclinic orbits start which end at other nodes. I never found heteroclinic orbits which do not end at internally stable patterns. Patterns which are also externally stable are terminating nodes in this net.

Starting with some random initial condition the system relatively quickly approaches the net. After that it ''travels'' on it from node to node. Each transition corresponds to a pattern switching. At the beginning the journey is still influenced by the randomness of the initial condition. But for increasing time the transition from one node to another one becomes more and more predictable. The reason for that is twofold. First, the angle-dependent growth rate $\lambda(\alpha)$ selects the fastest growing heteroclinic orbits. Second, the waiting time increases because the system approaches the heteroclinic orbits closer and closer. Thus the amplitudes of externally stable angles α [i.e., $\lambda(\alpha)<0$] relax to extremely low values [e.g., at $t=1000$ all amplitudes in Fig. 10(b) have values below 10^{-100} except the three amplitudes defining the pattern]. This increases the predictability of the selection

process because near the maximum of $\lambda(\alpha)$ the amplitudes have a Gaussian distribution, i.e.,

$$R_j(T) \approx R_j(0) e^{\lambda_{\max} T} \exp\left(\frac{\lambda''_{\max} T}{2} (\alpha_j - \alpha_{\max})^2 \right), \quad (68)$$

where the maximum and the curvature of the growth rate at $\alpha = \alpha_{\max}$ is denoted by $\lambda_{\max} > 0$ and $\lambda''_{\max} < 0$, respectively, T is the waiting time between two switchings, and the $R_j(0)$ are the values of the amplitudes after the last switch. We clearly see that the sharpness of the Gaussian distribution increases with T. For $T \to \infty$ the heteroclinic orbit is determined by $\alpha_{\max}$. The dynamics on the net becomes *deterministic* because there is always one single maximum of $\lambda(\alpha)$ which defines a unique heteroclinic orbit. The only exceptions are externally unstable squares because they have two equally sized maxima [see Fig. 6(b)]. Thus the values of the amplitudes at the angles of the maxima determine the heteroclinic orbit. I have found numerically that the heteroclinic orbit ends in a square if these amplitudes are of the same order. If a square pattern occurs the probability increases that the next switching will lead also to a square.

The dynamics can be described by a map of the angle space of the internally stable three-wave pattern onto itself. Up to an arbitrary rotation three-wave patterns are characterized by angle differences. For example, one can use $\alpha_2 - \alpha_1$ and $\alpha_3 - \alpha_2$ as in Fig. 9. Thus the map is two-dimensional. Not every internally stable three-wave pattern is mapped onto another internally stable three-wave pattern. There are three other possibilities. In each of them the dynamics is terminated in the sense that the trajectory on the net does not return to three-wave patterns. In the first case the pattern is externally stable. Thus a stable fixed point of the amplitude equations is reached. In the second case the pattern leads to a square. If squares are externally unstable, the system moves on the net from square to square. The motion is similar to the simple behavior of the system of three amplitude equation. Thus we get a quasiperiodic motion. In the third case, the three-wave pattern leads to a one-wave pattern. Looking at Fig. 6(a) it is clear that a one-wave pattern leads to another one-wave pattern rotated by roughly 45°.

I have numerically simulated this map. There are three steps. In a first step the pattern is calculated for a point in the plane $(\alpha_2 - \alpha_1, \alpha_3 - \alpha_2)$ which belongs to an internally stable three-wave pattern. In the second step the maximum of the growth rate $\lambda(\alpha)$ is searched. In the third step the amplitude equations are integrated numerically for a four-dimensional subspace defined by the amplitudes of the angles $\alpha_1 \equiv 0$, α_2, α_3, and $\alpha_{\max}$. For the initial value of $R_{\max}$ a small number, say 0.01, is chosen. This loop is repeated until one of the above-mentioned termination conditions is reached.

For the coupling functions of Figs. 10(b) and 10(c) I have often found very long transients (several hundred iterations) until the dynamics of the map is terminated. These transients are chaotic. I have seen this by looking at the distance between the trajectories of two slightly different initial conditions. The distance clearly increases roughly exponentially as long as it is much smaller than the possible maximum.

B. Dynamics with noise

In this subsection we investigate the amplitude dynamics in the presence of Gaussian white noise, i.e.,

$$\tau_0 \dot{R}_j = \epsilon R_j - c \left[R_j^2 + \sum_{j' \neq j} a(\alpha_j - \alpha_{j'}) R_{j'}^2 \right] R_j + \nu \xi_j(t) \quad (69)$$

with

$$\langle \xi_j(t) \rangle = 0, \quad \langle \xi_j(t) \xi_{j'}(t') \rangle = \delta(t - t') \delta_{j,j'}. \quad (70)$$

In a system with a Lyapunov functional, noise is necessary to bring the system from a metastable state to the ground state. In our case where a Lyapunov potential does not exist, a qualitatively similar behavior may occur. That is, noise may drive the system into some preferred state. Therefore I have integrated (69) for the coupling function of Fig. 9(a) where k_c is small and the number of stable three-wave patterns is large. For $\nu < 10^{-2} \sqrt{\epsilon^3 / c}$ the system behaves qualitatively as in the deterministic case discussed in the previous subsection. For $\nu > 10^{-2} \sqrt{\epsilon^3 / c}$ the probability for squares increases. The reason for that is twofold. First, some of the squares are not genuine squares. They are rhombic forming an angle which is not from the small interval around 90° mentioned in Sec. V B. These rhombic patterns are noisy three-wave patterns located in the angle space near the boundary of existence [see Fig. 9(a)]. One of the amplitudes of such patterns is of the same order as the noise amplitude. In the simulation shown in Fig. 11(a) an example of a rhombic pattern appears for t between 600 and 800. One clearly sees that the averaged noise level for the amplitudes $R_1, \ldots, R_{18}$ is larger than for $R_{20}, \ldots, R_{35}$. If we would switch off the noise, one of the amplitudes $R_1, \ldots, R_{18}$ would reach a nonzero value.

The second reason for a larger probability of squares is that sometimes a noise-induced pattern switching occurs which replaces the initial three-wave pattern by a three-wave pattern which is closer to the border of existence in the angle space. Thus noise drives the system in such a way that it prefers squares or rhombic patterns which are almost squares. Squares are more stable than rhombic patterns which are more stable than three-wave patterns. For $\nu > 0.1 \sqrt{\epsilon^3 / c}$ even squares becomes unstable. In Fig. 11(a) we clearly see squares and rhombic patterns which are followed by irregular noisy bursts where the noise is amplified. After a burst there follows again a square or a rhombic pattern. Note that these pattern changes are different from the pattern switching discussed in the previous subsection. Here the patterns perform a random walk on the circle whereas in the case of pattern switching the pattern drifts in a well-defined direction.

Nevertheless this drift is extremely sensitive to noise. In the previous subsection we have seen that the pattern-switching map becomes deterministic if the waiting time T is large. From (68) we see that T is related to the values of the amplitudes after the last switch. In the case of noise the amplitudes cannot decay on average below a level which is proportional to the noise amplitude. Thus the averaged waiting time is proportional to the logarithm of the inverse noise

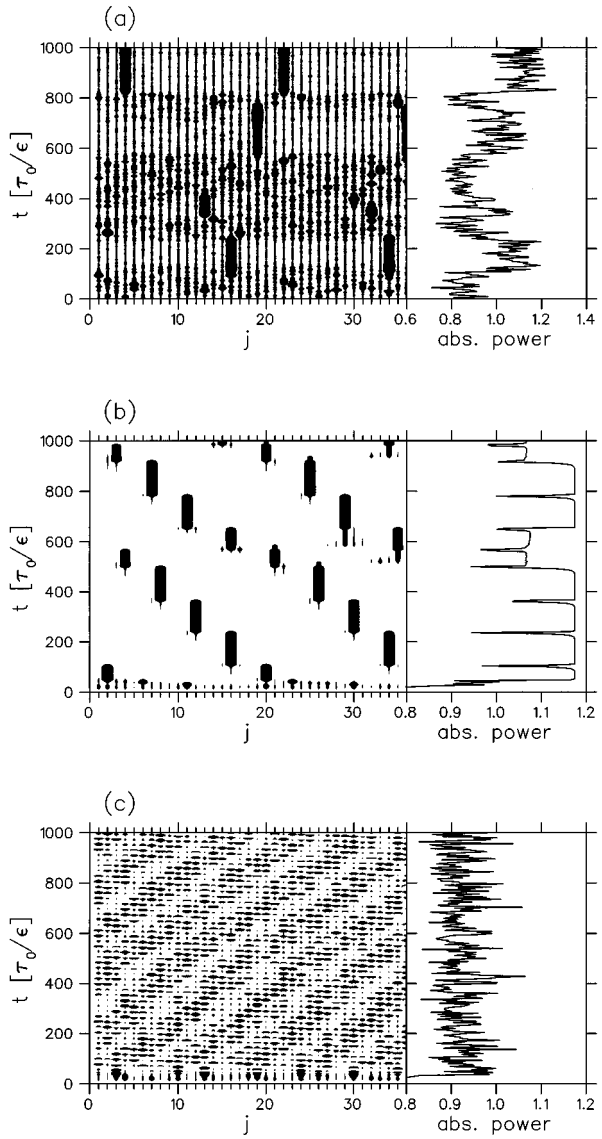

FIG. 11. The dynamical behavior of a system of 36 amplitude equations with noise. The parameters are the same as in Fig. 10. The noise levels are (a) $\nu=0.13\sqrt{\epsilon^3/c}$ and (b) and (c) $\nu=5\times10^{-7}\sqrt{\epsilon^3/c}$.

amplitude. Pattern switching therefore disappears if the averaged waiting time is of the same order as the averaged switching time.

Figure 11(b) shows an example of a simulation with a noise level which is by orders of magnitude smaller than the noise level of the simulation shown in Fig. 11(a). The coupling function is the same as for Fig. 10(b). Again we see that the drift caused by pattern switching and, as expected, the waiting time does not increase. Squares are much more probable than in the noiseless case. On the other hand there are noise-induced switchings from squares to three-wave patterns, a process which is very unlikely in the deterministic case. The stable three-wave patterns are robust against that noise level. It is not clear whether the behavior shown in Fig. 11(b) is a transient or not. In simulations of the kind shown in Fig. 11(b) I have never found a case in which the system selects a stable pattern.

Figure 11(c) shows a simulation for the same coupling function as for Fig. 10(c) and Fig. 9(c). Here all stationary patterns are unstable. The noise level is the same as in Fig. 11(b) but $\lambda_{\max}$ is often larger. Thus in accordance with (68) the averaged waiting time is smaller. It is almost of the same order as the switching time. A careful inspection of Fig. 11(c) shows that a fuzzy square drifts very fast clockwise around the circle. The anticlockwise rotation seen in Fig. 11(c) is an optical illusion caused by the finite number of amplitudes.

VII. CONCLUSION

In this work a system of amplitude equations for the out-of-plane parallel pumping has been derived [Eqs. (49)]. Internal anisotropy fields and surface pinning of spins have been neglected, but the dipolar field has been fully included. The dipolar field has two important consequences. (i) It is the main factor determining the most unstable mode. Corrections due to the exchange field are of second order. (ii) It gives rise to a strong odd contribution in the nonlinear coupling function $a(\alpha)$. In fact, without the dipolar field a would be a constant plus a very small even term caused by the exchange interaction.

The coupling function has been calculated numerically and analytically. It determines the dynamical behavior of the system of amplitude equations. Squares and periodic as well as quasiperiodic three-wave patterns are the only stable stationary patterns. Figure 8 shows how these patterns would look if visualized by Faraday rotation. These patterns become unstable if the critical wave number k_c determined by the parametric resonance condition $\omega/2=\omega_k^{(0)}=\omega_H-1+k/2+\mathcal{O}(k^2)$ exceeds a threshold. Near and above this threshold the dynamics is characterized by pattern switching. That is, an internally stable pattern, e.g., a square, is switched off and at the same time another internally stable pattern is switched on. This process is extremely sensitive to noise and leads to noise-induced weak turbulence.

Quadratic terms in the amplitude equation are absent because the system is symmetric against reflection at the middle plane of the film. In a real film this symmetry is often broken. Thus weak quadratic terms should be expected. Quadratic terms also appear near hybridization points where due to a strong coupling the threshold of the dipolar mode is increased to values which are above the threshold of the most unstable odd mode. Quadratic terms lead to hexagonal patterns and to secondary instabilities where these patterns become unstable.[1]

What may be expected if crystal-field anisotropies and surface pinning are included in the theory? A uniaxial anisotropy which does not destroy the rotational symmetry leaves the system of amplitude equations unchanged. Only the coupling function is slightly modified but still has the properties (50). This is also the case for surface pinning. If the spins pin differently at the lower and the upper surface, quadratic terms should appear. Cubic anisotropies destroy the rotational symmetry. There are two special cases. (i) The film surface is parallel to the (1,0,0) plane. Only in this case the linearized equation of motion (14) is not changed and *all* waves with an in-plane wave number k_c become still unstable simultaneously. But the coupling no longer depends on the angle differences alone. This may lead to a preference

of square patterns. (ii) The film surface is parallel to the (1,1,1) plane. The number of amplitude equations reduces to three. The preferred pattern may be hexagonal.

Amplitude equations are very successful in order to understand pattern formation in systems with strong dissipation. In the case of parametric resonance where the damping is relatively weak, amplitude equations may not be the optimal way to treat these systems. This is due to the fact that the third-order terms of the amplitude equations at the minimum of the neutral curve are presumably of the same strength as the fifth-order terms. The calculation of the fifth-order terms is straightforward but extremely tedious. The *S* theory does not have this problem because it is a multiple-scale expansion where the pump field is the expansion parameter. Thus the relative control parameter ϵ should not be small. Only the threshold has to be small which implies small damping. But the main problem of the *S* theory is that the damping is included only phenomenologically after the multiple-scale expansion of the undamped problem. It is an open question whether it possible to get the linear and nonlinear damping terms of the *S* theory systematically.

An experimentalist wants to know whether such patterns can be observed in a real experiment. In order to visualize them it is important to know how strongly a pattern changes the orientation of the polarization of the transmitted light. Faraday rotation at normal incidence measures the time-averaged z component of the magnetization integrated over the film thickness. Thus thicker films are better than thin films. Because the deviation of $\mathbf{M}$ from $M_0\mathbf{e}_z$ will be small, the deviation of the polarization of the light from its orientation in the case of the undriven film is proportional to the square of the opening angle θ of the precession cone. For YIG films of a few μm thickness precession cones with $\theta=5°$ can be detected.[8] In leading order of the amplitudes, the precession angle θ is given by

$$\theta(x,y)=4\langle|\mu|\rangle_{t,z}\left|\sum_j e^{i\alpha_j}R_j\cos(\mathbf{k}_j\mathbf{r}+\chi_j)\right|, \qquad (71)$$

where $\langle\ \rangle_{t,z}$ is the average with respect to t and z. For regular periodic patterns the maximum of θ can be calculated. For small values of k_c the maximum scales with the square root of $k_c\epsilon$.

In the Introduction I have already emphasized the important role of pattern visualization in order to understand the nonlinear behavior. Global information like the absorbed power is ambiguous. This is illustrated in Figs. 10 and 11 where the evolution of each amplitude is compared with the absorbed power which is proportional to the sum of the amplitudes squared. Sometimes it seems to be possible to identify from the absorbed power signal the pattern. For example the absorption is stronger for squares than for three-wave patterns [see Fig. 11(b)]. But this identification works only after a learning process where, first, some pattern has been identified and, second, a correlation between pattern and global information has been found. The same is true for other features of the dynamical process. For example, the absorbed power sharply decreases during a pattern switching process. A similar phenomenon occurs in Rayleigh-Bénard convection during the appearance or disappearance of a defect where the Nusselt number which measures heat flow also sharply decreases.[36]

We do not know which patterns and pattern dynamics lead to certain actually measured time behavior of the absorbed power. In the literature one often finds models which are simplifications like the Lorenz equation which is a simplification of Rayleigh-Bénard convection. That is, a small number of modes are assumed to be the most relevant degrees of freedom. Even though the models are often based on the *S* theory they are often not derived systematically. For example, the nonlinear coupling constants are not calculated. They are chosen in such a way that the nonlinear dynamics of the model fits at least qualitatively with the observed data. A systematic calculation of the coefficients would improve these models, but it would not help much because Lorenz-like models neglect often important degrees of freedom. From the theoretical point of view it is difficult to get them. It is relatively easy only near the main-pattern forming instability.

I would like to strongly encourage experimentalists to perform experiments where the patterns caused by parametrically excited spin waves can be directly observed. This step is absolutely essential in order to make progress in the understanding of the nonlinear dynamics of high-power ferromagnetic resonance. Theoretical works like the present one hopefully lead to a strong motivation which is needed to overcome the experimental difficulties of visualization.

ACKNOWLEDGMENTS

I gratefully acknowledge helpful discussions with H. Benner, W. Just, H. Riecke, G. and H. Sauermann. I especially thank H. Thomas for careful reading of the manuscript. This work was finished during my stay at the Technische Hochschule Darmstadt. I thank H. Sauermann for his hospitality. This work was supported by the Swiss National Science Foundation. A part of this work was performed within a program of the Sonderforschungbereich 185 Darmstadt-Frankfurt.

APPENDIX A: EXACT SOLUTIONS OF THE LINEARIZED, UNDAMPED AND UNDRIVEN EQUATION OF MOTION

The linearized equations of motion (16) without damping and driving (i.e., $g=\omega_h=0$) reads

$$\begin{aligned}(\omega_H-1+l^2k^2-\omega_k)\mu-l^2\mu''-\psi=0,\\ (\omega_H-1+l^2k^2+\omega_k)\mu^*-l^2\mu^{*\prime\prime}-\psi=0,\\ \psi''-k^2\psi-k^2(\mu+\mu^*)/2=0,\end{aligned} \qquad (A1)$$

with

$$\begin{aligned}\mu'(0)=\mu^{*\prime}(0)=\psi'(0)-k\psi(0)=0,\\ \mu'(1)=\mu^{*\prime}(1)=\psi'(1)+k\psi(1)=0.\end{aligned} \qquad (A2)$$

The boundary conditions for ψ come from integrating (16c) outside the interval $[0,1]$ and matching the exterior values of ψ and ψ' with its interior values at the boundary.

The general solution of (A1) is an arbitrary linear combination of the six eigenfunctions

$$\begin{pmatrix} \mu \\ \mu^* \\ \psi \end{pmatrix} = \begin{pmatrix} \mu_0 \\ \mu_0^* \\ \psi_0 \end{pmatrix} e^{iqz},$$

where q is a solution of the characteristic polynomial

$$(k^2+q^2)([\omega_H - 1 + l^2(k^2+q^2)]^2 - \omega_k^2) - k^2[\omega_H - 1 + a(k^2+q^2)] = 0. \tag{A3}$$

Because the general solution has to fulfill the six boundary conditions (A2), the coefficients of the eigenfunctions are the nontrivial solutions of a linear homogeneous system of algebraic equations. The determinant of the corresponding matrix has to be zero. This defines an implicit equation for ω_k. The determinant factorizes because (A1) and (A2) are invariant under inversion at $z=1/2$. Thus

$$\begin{pmatrix} \mu \\ \mu^* \\ \psi \end{pmatrix} = \sum_{j=1}^{3} C_j f_j(z) \begin{pmatrix} 1/\Delta\omega_j^- \\ 1/\Delta\omega_j^+ \\ 1 \end{pmatrix}, \tag{A4}$$

with

$$\Delta\omega_j^{\pm} = \omega_H - 1 + l^2(k^2+q_j^2) \pm \omega_k, \tag{A5}$$

$$f_j(z) = \begin{cases} q_j \cos\, q_j(z-1/2), & \text{for even solutions,} \\ \sin\, q_j(z-1/2), & \text{for odd solutions.} \end{cases} \tag{A6}$$

The boundary conditions $\mu'(0) = \mu^{*\prime}(0) = \psi'(0) - k\psi(0) = 0$ lead to

$$\begin{pmatrix} 1/\Delta\omega_1^- & 1/\Delta\omega_2^- & 1/\Delta\omega_3^- \\ 1/\Delta\omega_1^+ & 1/\Delta\omega_2^+ & 1/\Delta\omega_3^+ \\ 1-kh_1 & 1-kh_2 & 1-kh_3 \end{pmatrix} \begin{pmatrix} C_1 f_1'(0) \\ C_2 f_2'(0) \\ C_3 f_3'(0) \end{pmatrix} = 0, \tag{A7}$$

with

$$h_j = \begin{cases} q_j^{-1} \cot\, q_j/2, & \text{for even solutions,} \\ -q_j^{-1} \tan\, q_j/2, & \text{for odd solutions.} \end{cases} \tag{A8}$$

The zeros of the determinant of the matrix on the left-hand side of (A7) define ω_k which can be calculated numerically.

APPENDIX B: APPROXIMATED STABILITY ANALYSIS

The ansatz

$$\mu = (\mu_+ e^{i\omega t/2} + \mu_-^* e^{-i\omega t/2}) \cos N\pi z,$$

$$\mu^* = (\mu_- e^{i\omega t/2} + \mu_+^* e^{-i\omega t/2}) \cos N\pi z, \tag{B1}$$

together with Eq. (18) and $\lambda = 0$ turns (16a,16b) into

$$\begin{pmatrix} \alpha_- & \beta_N & \omega_h/2 & 0 \\ \beta_N & \alpha_+ & 0 & \omega_h/2 \\ \omega_h/2 & 0 & \alpha_+^* & \beta_N \\ 0 & \omega_h/2 & \beta_N & \alpha_-^* \end{pmatrix} \begin{pmatrix} \mu_+ \\ \mu_- \\ \mu_-^* \\ \mu_+^* \end{pmatrix} = 0, \tag{B2}$$

with

$$\alpha_{\pm} = \alpha_N \pm \frac{i\omega}{2(i \pm g)}, \tag{B3}$$

where α_N and β_N are defined by (24) and (22), respectively. The neutral curve is the smallest positive real solution of the characteristic polynomial in ω_h:

$$\omega_{h\mathrm{NC}}^{(N)}(k) = 2\sqrt{p_N - \sqrt{p_N^2 - q_N}}, \tag{B4}$$

with

$$p_N = \alpha_N^2 + \beta_N^2 - \frac{1-g^2}{(1+g^2)^2}\left(\frac{\omega}{2}\right)^2 \tag{B5}$$

and

$$q_N = \left(\alpha_N^2 - \beta_N^2 - \frac{\omega^2/4}{1+g^2}\right)^2 + \frac{\alpha_N^2}{(1+g^2)^2}\omega^2 g^2. \tag{B6}$$

The eigenvector is given by

$$\mu_{\pm} = \omega_h^3 - 2(\beta_N + \alpha_{\pm}^*)\omega_h^2 - 4[\beta_N^2 - (\alpha_{\pm} + \alpha_{\pm}^*)\beta_N + \alpha_{\pm}\alpha_{\mp}^*]\omega_h + 8(\beta_N^2 - \alpha_{\pm}^*\alpha_{\mp}^*)(\beta_N - \alpha_{\pm}), \tag{B7}$$

where ω_h is defined by (B4). The minimum of (B4) is

$$\omega_{hc}^{(N)} = \frac{\omega\alpha_N}{\beta_N} g + \mathcal{O}(g^2). \tag{B8}$$

It occurs at

$$\omega_k^{(N)} = \frac{\omega}{2} + \mathcal{O}(g^2), \tag{B9}$$

which is the condition for first-order parametric resonance. The eigenvector at the minimum is

$$\mu_{\pm} = 8\omega\alpha_N\left(\alpha_N - \beta_N \pm \frac{\omega}{2}\right)(1+i)g + \mathcal{O}(g^2). \tag{B10}$$

APPENDIX C: CALCULATION OF THE NONLINEAR COEFFICIENTS FOR $k_c \to 0$

In order to calculate $a(\alpha)$ we take in (33) only two amplitudes, say $A_{\pm}$ with $\alpha_{\pm} = \pm\alpha/2$ and $\mathbf{k}_{\pm} = k(\cos(\alpha/2)\cdot\mathbf{e}_x \pm \sin(\alpha/2)\cdot\mathbf{e}_y)$. The projection of $\mathbf{f}_3$ onto $\mathbf{u}_+^{\dagger}$ defined by (38) with $\mathbf{k}_j = \mathbf{k}_+$ and $\alpha_j = \alpha/2$ gives

$$\frac{\langle \mathbf{u}_+^{\dagger} | \mathbf{f}_3 \rangle}{S_h \omega_{h\mathrm{NC}}} = -c[|A_+|^2 + a(\alpha)|A_-|^2]A_+. \tag{C1}$$

In the limit $k \to 0$ the dipolar mode becomes independent of z, i.e.,

$$\mu(z,t)=\mu(t) \quad \text{and} \quad \psi(z,t)=-\frac{k}{4}[\mu(t)+\mu^*(t)]. \tag{C2}$$

The last equation is obtained from (18). The solution of (32) for $n=2$ becomes therefore simply

$$m_2=m_2^*=0, \quad \partial_z\phi_2=-2|m_1|^2B(z). \tag{C3}$$

The nonlinear terms of the third-order inhomogeneity $\mathbf{f}_3$ reads

$$-\begin{pmatrix} (i-g)\left[\frac{m_1^2}{2}(\partial_x-i\partial_y)\phi_1-2m_1|m_1|^2\right] \\ (-i-g)\left[\frac{m_1^{*2}}{2}(\partial_x+i\partial_y)\phi_1-2m_1^*|m_1|^2\right] \\ [(\partial_x+i\partial_y)m_1^*|m_1|^2+\text{c.c.}]B(z) \end{pmatrix}. \tag{C4}$$

We have dropped the exchange terms because they contribute only in second order of k. For the projection onto $\mathbf{u}_+^\dagger$ we have to calculate only the term of (C4) which is proportional to $\exp(i\mathbf{k}_+\mathbf{r})$. After some tedious calculations we get

$$\langle \mathbf{u}_+^\dagger|\mathbf{f}_3\rangle = 6\text{Re } w[|A_+|^2+a(\alpha)|A_-|^2]A_+,$$

where a is given by (54) with

$$a_s=\frac{2\text{Im } w}{3\text{Re } w} \tag{C5}$$

and

$$w=\langle \mu^2(t)[2\mu(-t)\mu^*(t)+\mu(-t)\psi(t)+\psi(-t)\mu^*(t)]\rangle_t, \tag{C6}$$

where $\langle\ \rangle_t$ denotes the temporal average. For c we get

$$c=\frac{-6\text{Re } w}{S_h\omega_{hc}}. \tag{C7}$$

Using (B10) one finds that at the minimum of the neutral curve w is purely imaginary in leading order. This has two consequences. (i) c changes its sign near the minimum of the neutral curve. (ii) a_s scales like $1/g$. Calculating the next-order terms we get (55) plus terms of order g^0.

APPENDIX D: REGULAR *N*-WAVE PATTERN

Regular N-wave patterns are characterized by equally spaced evenly angles α_j. That is,

$$\alpha_j=\frac{\pi}{N}j. \tag{D1}$$

Furthermore all amplitudes P_j are equal. Using (50) and (60) we get

$$P_j=P\equiv\frac{1}{\Sigma_{j=1}^N a(\pi j/N)-1}. \tag{D2}$$

It is convenient to introduce the Fourier series of the coupling function $a(\alpha)$:

$$a(\alpha)=\sum_{n=-\infty}^{\infty} a_n e^{2in\alpha}, \quad \text{with } a_{-n}=a_n^*. \tag{D3}$$

The Fourier coefficients are given by

$$a_n=\frac{1}{\pi}\int_0^\pi a(\alpha)e^{-2in\alpha}d\alpha. \tag{D4}$$

For $k_c\to 0$ where $a(\alpha)$ is very well approximated by (54), the Fourier components are

$$a_0=\frac{4}{3}, \quad a_1=\frac{1}{3}-i\frac{a_s}{2}, \quad a_{n>1}=0. \tag{D5}$$

Using the identity

$$\sum_{j=1}^N a\left(\frac{\pi}{N}j\right)e^{-2\pi i(m/N)j}=N\sum_{n=-\infty}^{\infty} a_{m+nN}, \tag{D6}$$

we can express P also in terms of the Fourier components of $a(\alpha)$

$$P=\frac{1}{N\Sigma_{n=-\infty}^{\infty}a_{nN}-1}. \tag{D7}$$

Regular N-wave patterns exist if P is positive. In the limit $k_c\to 0$ all regular patterns exist because of

$$P=\frac{3}{4N-3}>0, \quad \text{for } N>1. \tag{D8}$$

In the general case regular patterns will exist at least for large N if a_0 is positive and $a(\alpha)$ is a smooth function. In fact it is sufficient that the coupling function does not have steps which would lead to $|a_n|\sim 1/n$. For all numerically calculated coupling functions I have always found that $a(\alpha)$ is continuous and $a_0>0$. Moreover, all regular N-wave pattern exist because $a(\alpha)$ is always smooth enough.

In order to test the internal stability of the regular patterns, the eigenvalue problem (61) has to be solved. This can be done by the ansatz

$$C_j=e^{2\pi i(m/N)j}, \quad m=0,1,\ldots,N-1. \tag{D9}$$

Using (D6) we get the eigenvalues

$$\lambda_m=P\left(1-N\sum_{n=-\infty}^{\infty} a_{m+nN}\right). \tag{D10}$$

Because of (D7) $\lambda_0=-1$ holds for any N. For continuous coupling functions regular N-wave patterns become eventually unstable if N gets large. In the long-wavelength limit where only two Fourier components are nonzero all patterns with $N>3$ are internally unstable. Hexagons (i.e., $N=3$) are just marginal. That is,

$$\lambda_{1,2}=\mp i\frac{a_s}{2}. \tag{D11}$$

Squares are stable because $\lambda_1=-1/5$.

In order to test the external stability of regular N-wave patterns we have to calculate (62) which yields

$$\lambda(\alpha)=1-NP\sum_{n=-\infty}^{\infty}a_{nN}e^{2inN\alpha}. \tag{D12}$$

By using (D7) we immediately verify (63). For $k_c\to 0$ any regular pattern is externally stable because only the Fourier components a_0 and a_1 are nonzero. In the general case of continuous coupling functions, regular patterns are externally stable if N is sufficiently large.

APPENDIX E: THREE-WAVE PATTERNS FOR $k_c\to 0$ AND $g\to 0$

We calculate the general three-wave pattern for the coupling function (54) with $a_s\to\infty$ (i.e. $g\to 0$). We introduce the abbreviations

$$u_3=a_s\sin 2(\alpha_2-\alpha_1),\quad v_3=\frac{4}{3}+\frac{2}{3}\cos 2(\alpha_2-\alpha_1) \tag{E1}$$

and the cyclic permutations of them. The amplitudes P_j are solutions of

$$\begin{pmatrix} 1 & v_3-u_3 & v_2+u_2 \\ v_3+u_3 & 1 & v_1-u_1 \\ v_2-u_2 & v_1+u_1 & 1 \end{pmatrix}\begin{pmatrix} P_1 \\ P_2 \\ P_3 \end{pmatrix}=\begin{pmatrix} 1 \\ 1 \\ 1 \end{pmatrix}, \tag{E2}$$

which are given by

$$P_1=\frac{u_1(u_1+u_2+u_3)}{D}+\mathcal{O}(a_s^{-1}) \tag{E3}$$

and its cyclic permutations. The denominator D is the determinant of the matrix in (E2). In leading order of a_s it is given by

$$D=u_1(u_1+u_2v_3)+\text{cycl. perm.} \tag{E4}$$

Because v_j is always positive, we immediately see that $P_j>0$ for $j=1,2,3$ is only possible if all u_j's have the same sign. Thus the basic region of allowed angles is given by (65).

The general three-wave pattern is internally stable if the real part of each root of the characteristic polynomial defined by the determinant of the matrix of (61) is negative. The characteristic polynomial reads

$$\lambda^3+c_2\lambda^2+c_1\lambda+c_0=0 \tag{E5}$$

with

$$c_2=P_1+P_2+P_3,\quad c_0=P_1P_2P_3D \tag{E6}$$

and

$$c_1=P_2P_3(1-v_1^2+u_1^2)+\text{cycl. perm.} \tag{E7}$$

In accordance with the well-known Rough-Hurwitz criterion (see, e.g., Ref. 37) the real part of λ is always negative if and only if

$$c_2c_1>c_0>0. \tag{E8}$$

Since $P_j>0$ the last inequality leads to $D>0$ which is in leading order always fulfilled. Evaluating $c_2c_1-c_0$ in leading order of a_s shows that the first inequality also holds. Thus any possible three-wave pattern is internally stable.

[1] M. C. Cross and P. C. Hohenberg, Rev. Mod. Phys. **65**, 851 (1993).
[2] W. F. Brown, Jr., *Micromagnetics* (Wiley, New York, 1963).
[3] N. Bloembergen and R. W. Damon, Phys. Rev. **85**, 699 (1952).
[4] H. Suhl, J. Phys. Chem. Solids **1**, 209 (1957).
[5] P. E. Wigen, *Nonlinear Phenomena and Chaos in Magnetic Materials* (World Scientific, Singapore, 1994).
[6] Y. A. Gaidai, I. I. Kondilenko, and A. A. Solomko, Pis'ma Zh. Éksp. **21**, 575 (1975) [JETP Lett. **21**, 269 (1975)].
[7] W. Wettling, W. D. Wilber, P. Kabos, and C. E. Patton, Phys. Rev. Lett. **51**, 1680 (1983).
[8] K. Gnatzig, H. Dötsch, M. Ye, and A. Brockmeyer, J. Appl. Phys. **62**, 4839 (1987).
[9] M. Faraday, Philos. Trans. R. Soc. London **52**, 319 (1831).
[10] S. T. Milner, J. Fluid Mech. **225**, 81 (1991).
[11] F. J. Elmer, Phys. Rev. Lett. **70**, 2028 (1993).
[12] G. Küppers and D. Lortz, J. Fluid Mech. **35**, 609 (1969).
[13] F. H. Busse and K. E. Heikes, Science **208**, 173 (1980).
[14] F. J. Elmer, J. Magn. Magn. Mater. **140-144**, 1951 (1995).
[15] P. Manneville, *Dissipative Structures and Weak Turbulence* (Academics, Boston, 1990).
[16] V. E. Zakharov, V. S. L'vov, and S. S. Starobinets, Usp. Fiz. Nauk. **114**, 609 (1975) [Sov. Phys. Usp. **17**, 896 (1975)].
[17] V. S. L'vov, *Wave Turbulence Under Parametric Excitation* (Springer, Berlin, 1994).
[18] F. J. Elmer, Ph.D. thesis, Technische Hochschule Darmstadt, 1987.
[19] F. J. Elmer, J. Phys. (Paris) Colloq. **49**, C8-1597 (1988).
[20] F. J. Elmer, in *Pattern Formation in Complex Dissipative Systems*, edited by S. Kai (World Scientific, Singapore, 1992).
[21] F. Matthäus and H. Sauermann, Z. Phys. B **99**, 611 (1996).
[22] R. W. Damon, in *Magnetism*, edited by G. T. Rado and H. Suhl (Academic, New York, 1963), Vol. 1.
[23] D. A. Garanin, Physica A **172**, 470 (1991).
[24] T. Plefka, Z. Phys. B **90**, 447 (1993).
[25] M. Lakshmanan and K. Nakamura, Phys. Rev. Lett. **53**, 2497 (1984).
[26] Y. V. Gribkova and M. I. Kaganov, Fiz. Tverd. Tela **33**, 508 (1991) [Sov. Phys. Solid State **33**, 290 (1991)].
[27] B. A. Kalinikos, in *Linear and Nonlinear Spin Waves in Magnetic Films and Superlattices*, edited by M. G. Cottam (World Scientific, Singapore, 1994).
[28] We assume that $\omega>2(\omega_H-1)$ to ensure the existence of a mode which is able to fulfill the first-order parametric resonance condition.
[29] This is not true for a subcritical pitchfork bifurcation. Nevertheless, there will exist an unstable solution for which this property holds.
[30] A. Nayfeh, *Perturbation Methods* (Wiley, New York, 1973).
[31] The rotational symmetry is also responsible for the fact that the coupling function a depends only on the *difference* of the angles.
[32] L. D. Landau and E. M. Lifshitz, *Mechanics* (Pergamon, New York, 1960).

[33] The -1 in the dispersion relation (23) is actually the spatial-temporal average over $-M_z/M_0$ which decreases with increasing amplitudes A_j. To fulfill still the parametric resonance condition k has to be decreased. Thus the bifurcation on the lower(higher)-k side of the resonance dips in Fig. 2 is sub(super)critical.

[34] The correction in Ref. 11 which makes hexagons stable reads $-\eta+\eta\cos 2\alpha$, where $\eta=Dk_c^2/(9\pi)$ [note there is an error in Eq. (10) of Ref. 11]. This correction comes from the exchange interaction and is therefore of second order in k_c. But there is a first-order correction caused by the dipolar interaction which is responsible for the instability of hexagons.

[35] R. M. May and W. J. Leonard, SIAM J. Appl. Math. **29**, 243 (1975).

[36] V. Croquette, Contemp. Phys. **30**, 113, 153 (1989).

[37] J. M. T. Thompson and H. B. Stewart, *Nonlinear Dynamics and Chaos* (Wiley, New York, 1986).